

Tuning Frictional Properties of Kirigami Altered Graphene Sheets using Molecular Dynamics and Machine Learning

Designing a Negative Friction Coefficient

Mikkel Metzsch Jensen



Thesis submitted for the degree of
Master in Computational Science: Materials Science
60 credits

Department of Physics
Faculty of mathematics and natural sciences

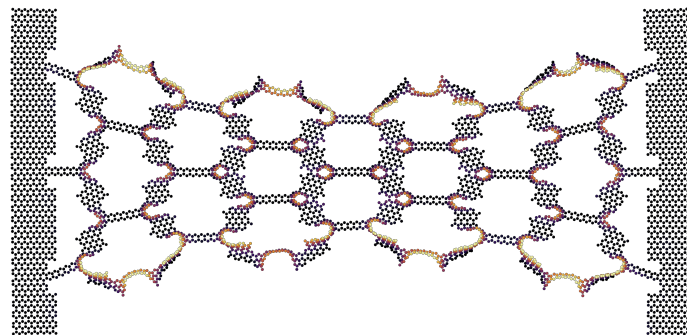
UNIVERSITY OF OSLO

Spring 2023

Tuning Frictional Properties of Kirigami Altered Graphene Sheets using Molecular Dynamics and Machine Learning

Designing a Negative Friction Coefficient

Mikkel Metzsch Jensen



© 2023 Mikkel Metzsch Jensen

Tuning Frictional Properties of Kirigami Altered Graphene Sheets using Molecular Dynamics and Machine Learning

<http://www.duo.uio.no/>

Printed: Reprocentralen, University of Oslo

Abstract

Abstract.

Acknowledgments

Acknowledgments.

List of Symbols

F_N Normal force (normal load)

Acronyms

AFM Atomic Force microscope. 21, 22, 23, 24

CM Center of Mass. 34, 35

FFM Friction Force Microscopes. 21, 22, 23, 24

FK Frenkel-Kontorova. 11, 16, 17, 18, 19, 20, 23, 24

FKT Frenkel–Kontorova–Tomlinson. 11, 20, 23, 24

GS Ground State. 17, 18

MD Molecular Dynamics. 2, 3, 10, 11, 12, 14, 23, 24, 25, 29, 30, 33, 42

ML Machine Learning. 2, 3, 30

PT Prandtl–Tomlinson. 11, 16, 17, 19, 20, 22, 24, 25

SFA Surface force apparatus. 22, 23

SFM Scanning Force Microscopies. 21

SPM Scanning Probe Microscopy. 21

std Standard Deviation. 36, 37, 40, 42

Contents

1	Introduction	1
1.1	Motivation	1
1.2	Goals	3
1.3	Contributions	3
1.4	Thesis structure	3
I	Background Theory	5
2	Friction	7
2.1	Friction across scales	7
2.2	Macroscale	7
2.2.1	Amontons' law	8
2.3	Microscopic scale	9
2.3.1	Asperity theories	9
2.4	Nanoscale — Atomic scale	10
2.4.1	Prandtl-Tomlinson	11
2.4.1.1	Thermal activation	12
2.4.1.2	Sliding speed	14
2.4.1.3	Tip mass	15
2.4.1.4	Friction Regimes: Smooth Sliding, Single Slip, and Multiple Slip	15
2.4.2	Frenkel-Kontorova	16
2.4.2.1	Commensurability	17
2.4.2.2	Velocity resonance	19
2.4.3	Frenkel-Kontorova-Tomlinson	20
2.4.4	Shortcomings of atomic models	21
2.4.5	Experimental procedures	21
2.4.5.1	Scanning Probe Microscopy	21
2.4.5.2	Surface Force Apparatus	22
2.5	Expected frictional properties of graphene	22
2.6	Research questions	25
II	Simulations	27
3	Pilot study	29
3.1	Friction simulation parameters	29
3.2	Force traces	30
3.2.1	Force oscillations	30
3.2.2	Decompositions	34
3.2.3	Center of mass path	34
3.3	Defining metrics for friction	36
3.3.1	Kinetic friction	36
3.3.2	Static friction	37

3.4	Out-of-plane buckling	38
3.5	Investigating main parameters	40
3.6	Load and stretch dependencies	42
3.6.1	Pressure reference for normal load	42
3.6.2	Contact area	42
3.6.3	Stretch	43
3.6.4	Normal force	45
3.7	Computational cost	46
	Appendices	47
	Appendix A	49
	Appendix B	51
	Appendix C	53

Chapter 1

Introduction

Structure of Motivation section:

1. Introduce and motivate friction broadly.
2. Motives for friction control using a grasping robot as example.
3. Analog to gecko feet where adhesive properties are turned on and off.
4. Interest in origin of friction through nanoscale studies which further motivates the use of MD.
5. Intro to metamaterials and the use of kirigami designs,
6. How to optimize kirigami designs with reference to Hanakata and motivating the use of ML.
7. Out-of-plane buckling motivates the use of kirigami for frictional properties.

Does some of the latter paragraphs belong to the approach section?

1.1 Motivation

Friction is a fundamental force that takes part in most of all interactions with physical matter. Even though the everyday person might not be familiar with the term *friction* we recognize it as the inherent resistance to sliding motion. Some surfaces appear slippery and some rough, and we know intuitively that sliding down a snow covered hill is much more exciting than its grassy counterpart. Without friction, it would not be possible to walk across a flat surface, lean against the wall without falling over or secure an object by the use of nails or screws [p. 5] [1]. It is probably safe to say that the concept of friction is integrated in our everyday life to such an extent that most people take it for granted. However, the efforts to control friction dates back to the early civilization (3500 B.C.) with the use of the wheel and lubricants to reduce friction in translational motion [2]. Today, friction is considered a part of the wider field *tribology* derived from the Greek word *Tribos* meaning “rubbing” and includes the science of friction, wear and lubrication [2]. The most compelling motivation to study tribology is ultimately to gain full control of friction and wear for various technical applications. Especially, reducing friction is of great interest as this has tremendous advantages for energy efficiency. It has been reported that tribological problems have a significant potential for economic and environmental improvements [3]:

“On global scale, these savings would amount to 1.4% of the GDP annually and 8.7% of the total energy consumption in the long term.” [4].

On the other hand, the reduction of friction is not the only sensible application for tribological studies. Controlling frictional properties, besides minimization, might be of interest in the development of a grasping robot where a finetuned object handling is required. While achieving a certain “constant” friction response is readily obtained through appropriate material choices during manufacturing, we are yet to unlock the capabilities to alter friction dynamically on the go. One example from nature inspiring us to think along these lines are the gecko feet. More precisely, the Tokay gecko has received a lot of attention in scientific studies aiming to unravel the underlying

mechanism of its “toggable” adhesion properties. Although geckos are able to produce large adhesive forces, they retain the ability to remove their feet from an attachment surface at will [5]. This makes the gecko able to achieve a high adhesion on the feet when climbing a vertical surface while lifting it for the next step remains relatively effortless. For a grasping robot we might consider an analog frictional concept of a surface material that can change from slippery to rough on demand depending on specific tasks.

In the recent years an increasing amount of interest has gone into the studies of the microscopic origin of friction, due to the increased possibilities in surface preparation and the development of nanoscale experimental methods. Nano-friction is also of great concern for the field of nano-machining where the frictional properties between the tool and the workpiece dictates machining characteristics [3]. With concurrent progress in computational power and development of Molecular Dynamics (MD), numerical investigations serve as an extremely useful tool for getting insight into the nanoscale mechanics associated with friction. This simulation based approach can be considered as a “numerical experiment” enabling us to create and probe a variety of high complexity systems which are still out of reach for modern experimental methods.

In materials science such MD-based numerical studies have been used to explore the concept of so-called *metamaterials* where material compositions are designed meticulously to enhance certain physical properties [6][7][8][9][10][11]. This is often achieved either by intertwining different material types or removing certain regions completely. In recent papers by Hanakata et al. [6](2018) [7](2020) numerical studies have showcased that mechanical properties of a graphene sheet, in this case yield stress and yield strain, can be altered through the introduction of so-called *kirigami* inspired cuts into the sheet. Kirigami is a variation of origami where the paper is cut additionally to being folded. While these methods originate as an art form, aiming to produce various artistic objects, they have proven to be applicable in a wide range of fields such as optics, physics, biology, chemistry and engineering [12]. Various forms of stimuli enable direct 2D to 3D transformations through folding, bending, and twisting of microstructures. While original human designs have contributed to specific scientific applications in the past, the future of this field is highly driven by the question of how to generate new designs optimized for certain physical properties. However, the complexity of such systems and the associated design space makes for seemingly intractable problems ruling out analytic solutions.

Earlier architecture design approaches such as bioinspiration, looking at gecko feet for instance, and Edisonian, based on trial and error, generally rely on prior knowledge and an experienced designer [9]. While the Edisonian approach is certainly more feasible through numerical studies than real world experiments, the number of combinations in the design space rather quickly becomes too large for a systematic search, even when considering the simulation time on modern day hardware. However, this computational time constraint can be relaxed by the use of machine learning (ML) which have proven successful in the establishment of a mapping from the design space to physical properties of interest. This gives rise to two new styles of design approaches: One, by utilizing the prediction from a trained network we can skip the MD simulations all together resulting in an *accelerated search* of designs. This can be further improved by guiding the search accordingly to the most promising candidates, as for instance done with the *genetic algorithm* which suggest new designs based on mutation and crossing of the best candidates so far. Another, even more sophisticated approach, is through generative methods such as *Generative Adversarial Networks* (GAN). By working with a so-called *encoder-decoder* network structure, one can build a model that reverses the prediction process. That is, the model predicts a design from a set of physical target properties. In the papers by Hanakata et al. both the *accelerated search* and the *inverse design* approach was proven successful to create novel metamaterial kirigami designs with the graphene sheet.

Hanakata et al. attributes the variety in yield properties to the non-linear effects arising from the out-of-plane buckling of the sheet. Since it is generally accepted that the surface roughness is of great importance for frictional properties it can be hypothesized that the kirigami cut and stretch procedure can also be exploited for the design of frictional metamaterials. For certain designs we might hope to find a relationship between stretching of the sheet and frictional properties. If significant, this could give rise to a variability of the friction response beyond manufacturing material choice. For instance, the grasping robot might apply such a material as artificial skin for which stretching or relaxing of the surface could result in a changeable friction strength; Slippery and smooth when in contact with people and rough and firmly gripping when moving heavy objects. In addition, a possible coupling between stretch and the normal load through a nanomachine design would allow for an altered friction coefficient. This invites the idea of non-linear friction coefficients which might in theory also take on negative values given the right response from stretching. The latter would constitute an extremely rare property. This has (**only?**) been reported indirectly for bulk graphite by Deng et al. [13] where the friction kept increasing during the unloading phase. **Check for other cases and what I can really say here.**

To the best of our knowledge, kirigami has not yet been implemented to alter the frictional properties of a nanoscale system. In a recent paper by Liefferink et al. [14](2021) it is reported that macroscale kirigami can be used to dynamically control the macroscale roughness of a surface through stretching which was used to change the frictional coefficient by more than one order of magnitude. This supports the idea that kirigami designs can in fact be used to alter friction, but we believe that taking this concept to the nanoscale regime would involve a different set of underlying mechanisms and thus contribute to new insight in this field.

1.2 Goals

In this thesis we investigate the possibility to alter and control the frictional properties of a graphene sheet through application of kirigami inspired cuts and stretching of the sheet. With the use of MD simulations we evaluate the friction properties under different physical conditions in order to get insight into the prospects of this field. By evaluating variations of two kirigami inspired patterns and a series of random walk generated patterns we create a dataset containing information of the frictional properties associated with each design under different load and stretch conditions. We apply ML to the dataset and use an accelerated search approach to optimize for different properties of interest. The subtask of the thesis are presented more comprehensively in the following.

1. Define a sheet indexing that allows for a unique mapping of patterns between a hexagonal graphene lattice representation to a matrix representation suited for numerical analysis.
2. Design a MD simulation procedure to evaluate the frictional properties of a given graphene sheet under specified physical conditions such as load, stretch, temperature etc.
3. Find and implement suitable kirigami patterns which exhibit out-of-plane buckling under tensile load. This includes the creation of a framework for creating variations within each pattern class. Additionally create a procedure for generating different styles of random walk patterns.
4. Perform a pilot study of a representative subset of patterns in order to determine appropriate simulation parameters to use for the further study along with an analysis of the frictional properties shown in the subset.
5. Create a dataset consisting of the chosen kirigami variations and random walk patterns and analyse data trends.
6. Train a neural network to map from the design space to physical properties such as mean friction, maximum friction, contact area etc. and evaluate the performance.
7. Perform an accelerated search optimizing for interesting frictional properties using the ML model. This should be done both through the pattern generation procedures and by following a genetic algorithm approach.
8. Use the most promising candidates from the accelerated search to investigate the prospects of creating a nanomachine setup which exhibits a negative friction coefficient.
9. Study certain designs of interest with the scope of revealing underlying mechanism. This includes simple correlation analysis but also a visualization of feature and gradient maps of the ML network.

Is the list of subtask too specific? Some of the details here might be better suited for the thesis structure section.

1.3 Contributions

What did I actually achieve

1.4 Thesis structure

How is the thesis structured.

Part I

Background Theory

Chapter 2

Friction

Friction plays a central role for the topic of this thesis being the key concept that we want to explore through the design of nanostructures. In this chapter we review the relevant theoretical understanding and highlight the derived expectations for our study.

Friction is a part of the wider field tribology which includes the study of friction, wear and lubrication between two surfaces in relative motion [1, p. 1]. In this thesis we will only concern ourselves with so-called wearless dry friction. That is, without any use of lubrication and without any resulting wear of the contacting surfaces.

2.1 Friction across scales

Tribological systems take place across a broad range of time and length scales, ranging from geological stratum layers involved in earthquakes [3] to atomistic processes, as in the gliding motion of a nanocluster or a nanomotor [15]. This vast difference in scale gives rises to different frictional mechanism being dominating. On a macro scale the system is usually subject to a relatively high load and sliding speed leading to a high contact stress and wear. On the other hand, the micro-/nanoscale regime occupies the opposite domain operating under relatively small load and sliding speed with negligible wear [3] [2, p. 5]. While macroscale friction is often reduced into a few variables such as load, material type, sliding speed and surface roughness, it is clear that the micro-/nanoscale friction cannot be generalized under such a simple representation. On the micro-/nanoscale the tribological properties are dominated by surface properties which will yield a more complex behaviour of said variables and introduce an additional sensitivity to variables such as temperature, humidity and even sliding history. The works of Bhushan and Kulkarni [16] showed that the friction coefficient decreased with scale even though the materials used was unchanged. This reveals an intrinsic relationship between friction and scale as the contact condition is altered.

The phenomenological descriptions of macroscale friction cannot yet be derived from the fundamental atomic principles, and bridging the gap between different length scales in tribological systems remains an open challenge [15]. Hence, the following sections will be organized into macroscale (Sec. 2.2), microscale (Sec. 2.3) and nanoscale (Sec. 2.4) representing the theoretical understanding governing each scale regime. Realising that the field of tribology across all scales is a vastly broad and intricate topic, we will aim to introduce only the essential findings for each scale, while keeping a main focus on necessary theoretical background associated to the understanding of our system of interest which takes place at the lowest scale.

2.2 Macroscale

Our working definition of the *macroscale* is everything on the scale of visible objects. This is usually denoted to the size of millimeters 10^{-3} m and above. Most importantly, we want to make a distinction to the microscale, where the prefix indicates the size of micrometers m^{-6} . Hence, we essentially consider everything larger than *micro* to belong to the macroscale¹.

¹The width of a human hair is often used as a reference for the limit of human perception. Since the width of a human hair is on the length scale 10^{-5} to 10^{-4} m we find this limit aligns rather well with the defined transition from macro- to microscale.

2.2.1 Amontons' law

In order to start and keep a solid block moving against a solid surface we must overcome certain frictional forces F_{fric} [1]. The static friction force F_s corresponds to the minimum tangential force required to initiate the sliding while the kinetic friction force F_k corresponds to the tangential force needed to sustain such a sliding at steady speed. The work of Leonardo da Vinci (1452–1519), Guillaume Amontons (1663–705) and Charles de Coulomb (1736–1806) all contributed to the empirical law, commonly known as *Amontons' law*, which serves as a common base for macroscale friction. Amontons' law states that the frictional forces is entirely independent of contact area and sliding velocity. Instead, it relies only on the normal force F_N , acting perpendicular to the surface, and the material specific friction coefficient μ as

$$F_{\text{fric}} = \mu F_N. \quad (2.1)$$

Notice that the term *Normal force* is often used interchangeably with *load* and *normal load* although the latter two terms refer to the applied force, “pushing” the object into the surface, and the first is the reaction force acting from the surface on the object. In equilibrium, these forces are equal in magnitude and hence we will not make a distinction between these terms. On the same note, we point out that the frictional force is different from a conventional force which in the Newtonian definition acts on a body from the outside and make it accelerate [17]. Rather than being an independent external force the friction force is an internal *reaction* force opposing the externally applied “sliding” force.

The friction coefficient μ is typically different for the cases of static (μ_s) and kinetic (μ_k) friction, usually both with values lower than one and $\mu_s \geq \mu_k$ in all cases [1, p. 6]. The friction coefficient is taken to be a constant defined by either [17]

$$\mu_1 = \frac{F_{\text{fric}}}{F_N}, \quad (2.2a)$$

or

$$\mu_2 = \frac{dF_{\text{fric}}}{dF_N}. \quad (2.2b)$$

The first definition Eq. (2.2a) requires zero friction at zero load, i.e. $F_{\text{fric}} = 0$ at $F_N = 0$, while the second definition Eq. (2.2b) allows for a finite friction force at zero load as the coefficient is defined by the slope of the $F_{\text{fric}}-F_N$ -curve. The consequences of these definitions are illustrated in Fig. 2.1, for selected $F_{\text{fric}}-F_N$ -curves in Fig. 2.1a and corresponding friction coefficients in Fig. 2.1b and Fig. 2.1c. For adhesive contacts the friction force will not be zero under zero load (red curve: Linear + shift) which can be mitigated by adding an extra constant to Eq. (2.1) [17]. Using Eq. (2.2a) for adhesive contacts would make the friction coefficient diverge for decreasing load as illustrated in Fig. 2.1b. Thus, we find the second definition Eq. (2.2b) more robust and versatile. This also allows for a better interpretation of the friction coefficient in the hypothetical case where friction depends non-linearly on load (Purple curve in Fig. 2.1).

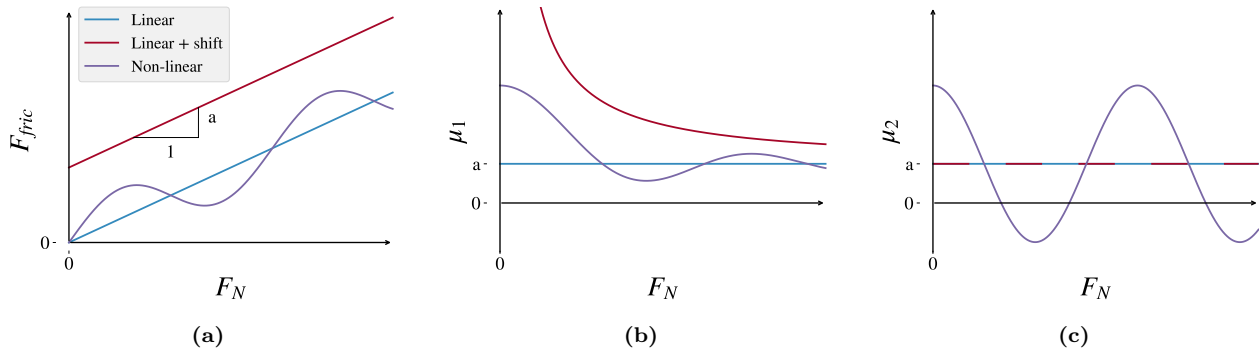


Figure 2.1: CAPTION

Although Amontons' law has been successful in its description of the majority of rubbing surfaces, involving both dry and lubricated, ductile and brittle and rough and smooth (as long as they are not adhesive) surfaces [17], it has its limitations. It is now known that Eq. (2.1) is not valid over a large range of loads and sliding velocities and that it completely breaks down for atomically smooth surfaces in strongly adhesive contact [17]. For instance, the independency of sliding velocity disappears at low velocities as thermal effects become important and for

high velocities due to inertial effects [1, pp. 5-6]. For the case of static friction, it was discovered to be dependent on the so-called contact history with increasing friction as the logarithm of time of stationary contact [18].

In cases where Amontons' law breaks down we might still use the conceptual definition of the friction coefficient as defined by (Eq. (2.2b)). Especially, in the context of achieving negative friction coefficients (in certain load ranges) we would refer to this definition, since Eq. (2.2a) would imply a truly unphysical situation of the frictional force acting in the same direction as the sliding motion. This would accelerate the object indefinitely².

Due to the empirical foundation of Amontons' law it does not provide any physical insight into the underlying mechanisms of friction. However, as we will later discuss in more detail, we can understand the overall phenomena of friction through statistical mechanics by the concept of *equipartition of energy* [15]. A system in equilibrium has its kinetic energy uniformly distributed among all its degrees of freedom. When a macroscale object is sliding in a given direction it is clearly not in equilibrium since one of its degrees of freedom carries considerable more kinetic energy. Thus, the system will have a tendency to transfer kinetic energy to the remaining degrees of freedom as heat which dissipates to the surroundings and making the object slow down if not continuously driven forward by an external energy source. Hence, we can understand the overall concept of friction simply as the tendency of going toward equilibrium energy equipartitioning among many interacting degrees of freedom [15]. From this point of view it is clear that friction is an inevitable part of contact physics, but even though friction cannot be removed altogether, we are still capable of manipulating it in useful ways.

The attentive reader might point out that we have already moved the discussion into the microscopic regime as *statistical mechanics* generally aim to explain macroscale behaviour by microscopic interactions. In fact, this highlights the necessity to consider smaller scales in order to achieve a more fundamental understanding of friction.

2.3 Microscopic scale

Going from a macro- to a microscale perspective, at a length scale on the order 10^{-6} m, it was realised that most surfaces are in fact rough [19]. The contact between two surfaces consists of numerous smaller contact points, so-called *asperities*, which form junctions due to contact pressure and adhesion as visualized in Fig. 2.2 [3]. In the macroscale perspective of Amonton's law we refer to time- and space-averaged values, i.e. the apparent contact area and the average sliding speed [17]. However, microscopically we find the real contact area to be much smaller than the apparent area [3], and the shearing motion of local microjunctions to happen at large fluctuations rather than as one synchronized movement throughout the surface.

It is generally accepted that friction is caused by two mechanisms: Mechanical friction and chemical friction [3]. The mechanical friction is the “plowing” of the surface by hard particles or said asperities with an energy loss attributed to deformations of the asperity. While plastic deformations, corresponding to wear, gives rise to an obvious attribution for the energy loss, elastic deformations are also sufficient in explaining energy loss due to phonon excitations. In fact the assumption of plastic deformations has been criticized as this is theorized only to be present in the beginning of a surface contact while it is negligible for prolonged or repeated contacts [20]. That is, when machine parts slide against each other for millions of cycles, the plastic deformation would only take place in the beginning for which the system then reaches a steady state with only elastic deformations. The chemical friction arises from adhesion between microscopic contacting surfaces, with an energy loss attributed to the breaking and forming of bonds.

2.3.1 Asperity theories

Asperity theories have their foundations in the adhesion model proposed by Bowden and Tabor [21] which is based on the fundamental reasoning that friction is governed by the adhesion between two surfaces [22]. Adhesion is proportional to the real contact area defined by asperity junctions and interfacial shear strength τ between such contacting junctions. For an asperity contact area A_{asp} we get a true contact area $\sum A_{\text{asp}}$ leading to

$$F_{\text{fric}} = \tau \sum A_{\text{asp}}.$$

²You would most likely have a good shot at the Nobel Prize with that paper.

Note that this is still compatible with Amontons' law in Eq. (2.1) by having a linear relationship between the real contact area and the applied load. In fact, this is exactly how the theoretical model explains the friction dependency of load. By increasing the normal load it is hypothesized that the real contact area will increase as the asperity tips are deformed (plastically or elastically) into broader contact points as visualized qualitatively in Fig. 2.2.

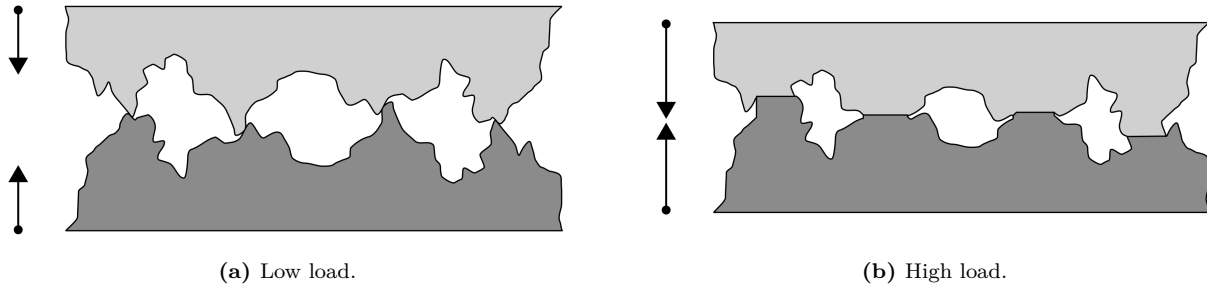


Figure 2.2: Qualitative illustration of the microscopic asperity deformation under increasing load from frame (a) to (b) [23]. While this figure seemingly portrays plastic deformation the concept of increased contact area under increased load applies for elastic deformation as well.

Many studies have focused on single asperity contacts to reveal the relationship between the contact area and load [24–26]. By assuming perfectly smooth asperities, with radii of curvature from micrometers all the way down to nanometers, continuum mechanics can be used to predict the deformation of asperities as load is applied. A model for non-adhesive contact between homogenous, isotropic, linear elastic spheres was first developed by Hertz [27], which predicted $A_{\text{asp}} \propto F_N^{2/3}$. Later adhesion effects were included in a number of subsequent models, including Maugis-Dugdale theory [28], which also predicts a sublinear relationship between A_{asp} and F_N . Thus, the common feature of all single-asperity theories is that A_{asp} is a sublinear function of F_N , leading to a similar sublinear relationship for $F_{\text{fric}}(F_N)$, which fails to align with the macroscale observations modelled by Amontons' law (eq. (2.1)).

Concurrently with single-asperity studies, roughness contact theories are being developed [29–32] to bridge the gap between single asperities and macroscopic contacts [19]. A variety of multi-asperity theories has attempted to combine single asperity mechanics by statistical modelling of the asperity height and spatial distributions [20]. This has led to a partially success in the establishment of a linear relationship between A_{asp} and F_N . Unfortunately, these results are restricted in terms of the magnitude of the load and contact area, where multi-asperity contact models based on the original ideas of Greenwood and Williamson [31] only predicts linearity at vanishing low loads, or Persson [30] which predicts linearity for more reasonable loads but only up to 10–15 % of the macroscale contact area. However, as the load is further increased all multi-asperity models predict the contact area to fall into the sublinear dependency of normal force as seen for single asperity theories as well [20].

2.4 Nanoscale — Atomic scale

Going from a micro- to a nanoscale, on the order of 10^{-9} m, it has been predicted that continuum mechanics will start to break down [33] due to the discreteness of individual atoms. In a numerical MD study by Mo et al. [19], considering asperity radii of 5–30 nm, it has been shown that the asperity area A_{asp} , defined by the circumference of the contact zone, is sublinear with F_N . This is accommodated by the observation that not all atoms within the circumference make chemical contact with the substrate. By modelling the real contact area $A_{\text{real}} = N A_{\text{atom}}$, where N is the amount of atoms within the range of chemical interaction and A_{atom} the associated surface area for a contacting atom, they found a consistent linear relationship between friction and the real contact area. Without adhesive forces this lead to a similar linear relationship $F_{\text{fric}} \propto F_N$, while adding van der Waals adhesion to the simulation gave a sublinear relationship matching microscale single asperity theory, even though the $F_{\text{fric}} \propto A_{\text{real}}$ was maintained. This result emphasizes that the predictions of continuum mechanics might still apply at the nanoscale and that the contact area can still be expected to play an

important role for nanoscale asperity contact. It is simply the definition of the contact area that undergoes a change when transitioning from micro- to nanoscale.

While the study by Mo et al. [19] considers a single asperity on a nanoscale, some models take this even further to what we will denote as the atomic-scale. This final leap is motivated by the fact that our system of interest, an atomically flat graphene sheet imposed on a flat silicon substrate, lacks the presence of nanoscale asperities in its initial uncut undeformed state. In the lack of noteworthy structural asperities, friction can instead be modelled as a consequence of the “rough” potential laid out by the atomic landscape. A series of so-called reduced-order models builds on a simplified system of atomic-scale contacts based on three essential parts: 1) A periodic potential modelling the substrate as rigid crystalline surface. 2) An interacting particle, or collection of particles, placed in the potential. 3) A moving body, moving at steady speed, and connected to the particles through a harmonic coupling. In figure Fig. 2.3 three of the most common 1D models is displayed which we will address in the following sections. The time-honored Prandtl-Tomlinson (PT) model describes a point-like tip sliding over a space-periodic fixed crystalline surface with a harmonic coupling to the moving body. This is analog to that of an experimental cantilever used for Atomic Force Microscopy which we will introduce in more details in Sec. 2.4.5.1. Further extensions was added in the Frenkel-Kontorova (FK) model by substituting the tip with a chain of harmonic coupled particles dragged from the end, and finally combined in the Frenkel-Kontorova-Tomlinson (FKT) with the addition of a more rigorous harmonic coupling between the moving body and each of the atoms in the chain. While these models cannot provide the same level of details as atomistic simulations such as MD it enables investigation of atomic friction under most conditions, some of which are inaccessible to MD [34]. This makes these models an appropriate tool for investigating individual parameters and mechanisms governing affecting friction.

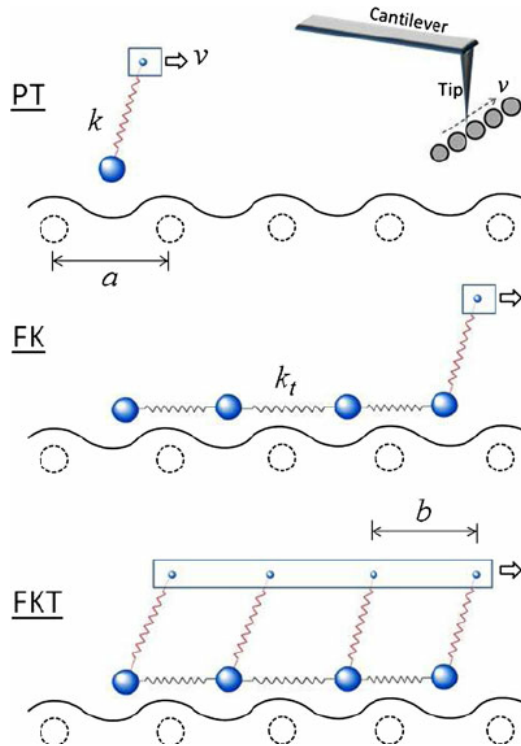


Figure 2.3: Temporary figure from [34]. Be careful to align notation on the figures with the text later on.

2.4.1 Prandtl–Tomlinson

We consider the Prandtl–Tomlinson model (PT) with added thermal activation as proposed by Gnecco et al. [35]. For the theoretical foundation of this section we generally refer to [34].

The 1D PT model assumes a single ball-tip coupled harmonically to a support moving at constant speed which makes the tip slide along the rigid substrate. The interaction between tip and substrate is modelled as a sinusoidal corrugation potential mimicking the periodicity found in a crystalline substrate. The total potential

energy is given as

$$V(x, t) = \frac{1}{2}K(vt - x)^2 - \frac{1}{2}U_0 \cos\left(\frac{2\pi x}{a}\right). \quad (2.3)$$

The first term describes the harmonic coupling at time t , with spring constant K , between the tip at position x and the moving body at position vt , given by its constant speed v . The second term describes the corrugation potential with amplitude U_0 and period a representing the lattice spacing of the substrate. The dynamics of the tip can be described by the Langevin equations

$$m\ddot{x} + m\mu\dot{x} = -\frac{\partial V(x, t)}{\partial x} + \xi(t), \quad (2.4)$$

Match notation with later use.

where m is the mass of the tip, μ the viscous friction and $\xi(t)$ the thermal activation term. The equation is solved for tip position x and the friction force is retrieved as the force acting on the moving body

$$F_{\text{fric}} = K(vt - x).$$

The governing equation Eq. (2.4) belongs to a family of stochastic differential equations composed of deterministic dynamics and stochastic processes. In this case the deterministic term is the viscous friction, $m\mu\dot{x}$, to resist the movement of the tip and the force acting from the corrugation potential. The stochastic term is a random force field modelling thermal noise according to the fluctuation–dissipation relation. Thus, there is no single path but rather multiple paths the tip can take. While the Langevin equations is one of the most common ways to handle thermal activaiton other methods exist to solve this problem such as Monte Carlo sampling methods. We ommit the numerical scheme for solving this and refer to a more in depth discussion of the Langevin equations with respect to the use in MD simulations in ??.

2.4.1.1 Thermal activation

The solving of the Langevin equations, as opposed to Newtons equation of motion, introduces thermal effects to the system. Generally, when the energy barrier comes close to $k_B T$ (0.026 eV at room temperature) thermal effects can not be neglected. In the case of a single asperity contact the energy barrier is on the order 1 eV which make thermal activation significant [34]. Due to the moving body travelling at constant speed the potential energy will increase steadily. Without any temperature, $T = 0$, the slip will only accour when the energy barrier between the current potential well (i) and the adjacent (j) is zero $\Delta V_{i \rightarrow j} = 0$. However, in the presence of temperature we get thermal activation, meaning that the tip can slip to the next potential well sooner $\Delta V_{i \rightarrow j} > 0$. Provided that the sliding speed is slow enough (Elaborate) the transistion rate κ for a slip from the current to the next well is given by

$$\kappa = f_0 e^{-\Delta V/k_B T}, \quad (2.5)$$

with ΔV being the energy barrier and f_0 the attempt rate. The attempt rate following Kramer's rate theory [36] is related to the mass and damping of the system and can be thought of as the frequency which the tip “attempts” to overcome the barrier. Notice that Eq. (2.5) resembles a microstate probability in the canonical ensemble with f_0 in place of the inverse partion function Z^{-1} which can be used as another intepretation of f_0 . The probability p_i that the tip occupies the current well i relative to the adjacent well j , as illustrated in Fig. 2.4 is governed by

$$\frac{dp_i}{dt} = -\kappa_{i \rightarrow j} p_i + \kappa_{j \rightarrow i} p_j.$$

This probability is related to temperature, speed and mass.

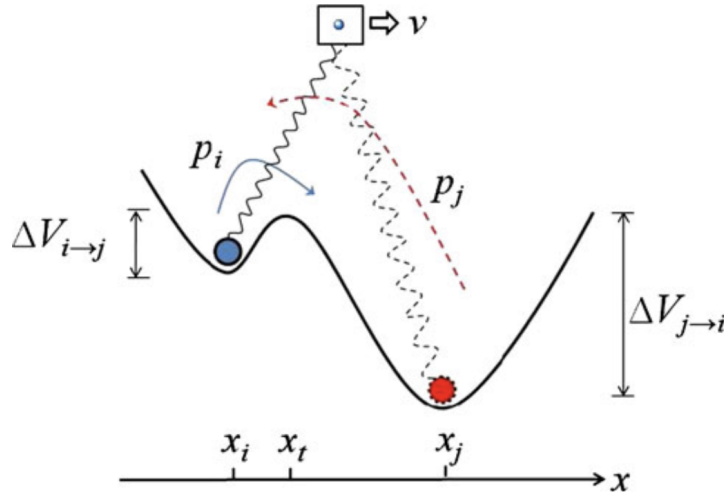


Fig. 3 An illustration of slip between two adjacent energy minima. p_i is the probability of the tip residing in the current potential well, i , where the energy barrier is $\Delta V_{i \rightarrow j}$. p_j is the probability of the tip residing at the next minima, j , where $\Delta V_{j \rightarrow i}$ is the corresponding energy barrier

Figure 2.4: [Temporary] figure from [34]

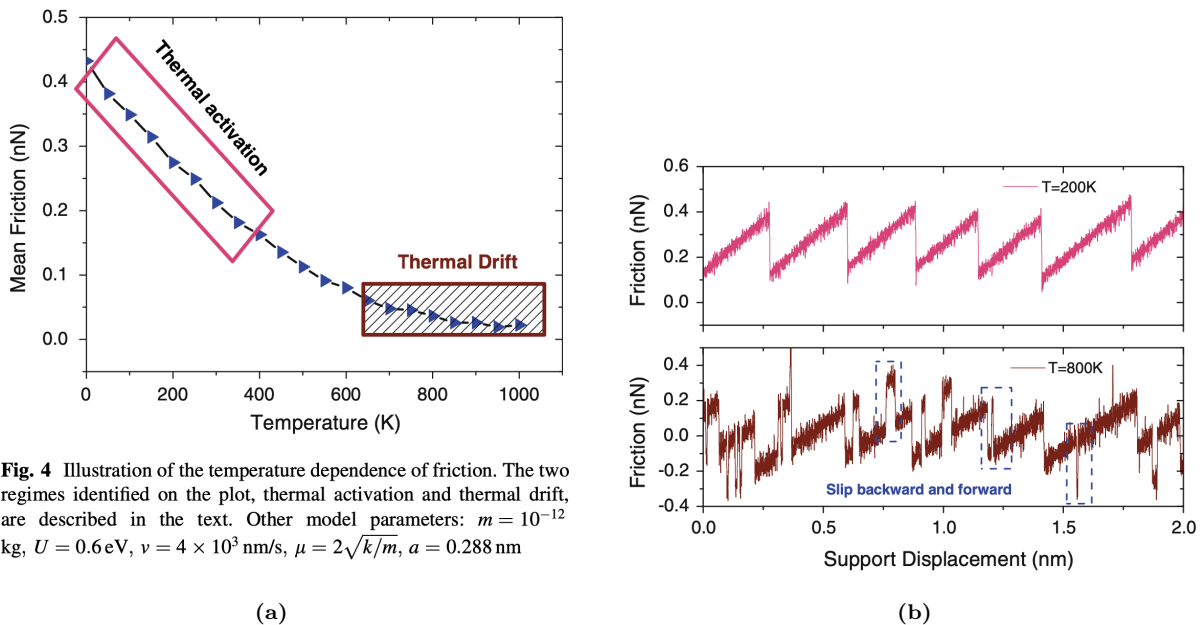


Fig. 4 Illustration of the temperature dependence of friction. The two regimes identified on the plot, thermal activation and thermal drift, are described in the text. Other model parameters: $m = 10^{-12}$ kg, $U = 0.6$ eV, $v = 4 \times 10^3$ nm/s, $\mu = 2\sqrt{k/m}$, $a = 0.288$ nm

Figure 2.5: [Temporary] figures from [34]

Generally, there exist two temperature regimes in the model: Thermal activation at low temperature and thermal drift at high temperature as shown in Fig. 2.5. At lower temperature the system is subject to standard thermal activation with $\Delta V_{i \rightarrow j} \gg \Delta V_{j \rightarrow i}$ resulting in $\kappa V_{i \rightarrow j} \gg \kappa V_{j \rightarrow i}$. Effectively, this inhibits any backwards

slip and we get

$$\frac{dp_i}{dt} = -\kappa_{i \rightarrow j} p_i,$$

which make the relationship between friction, temperature and speed follow Sang et al.'s prediction [37]

$$F = F_c - \left| \beta k_B T \ln \left(\frac{v_c}{v} \right) \right|^{2/3}, \quad v_c = \frac{2f_0 \beta k_B T}{3C_{\text{eff}} \sqrt{F_c}}, \quad (2.6)$$

where F_c is the maximum friction at $T = 0$, v_c a critical velocity, f_0 is the attempt rate, C_{eff} the effective stiffness, and β a parameter determined by the shape of the corrugation well. Eq. (2.6) characterizes the decrease in friction with temperature in the thermal activation regime, shown in Fig. 2.5a at low temperature, with the assumption of only forward slips, as seen in the force trace shown in Fig. 2.5a. When the temperature is high enough, for the system to be consistently close to thermal equilibrium, it enters the regime of thermal drift [38]. This regime transition can be understood through a comparison of two time scales: The time it takes for the moving body to travel one lattice spacing $t_v = a/v$ and the average time for a slip to occur due to thermal activation $\tau = 1/\kappa = f^{-1} \exp(\Delta V/k_B T)$. If $t_v \gg \tau$ the system falls within the thermal drift regime, with slips both backwards and forwards as shown in Fig. 2.5b, and the friction follows the prediction of Krylov et al. [38–40]

$$F \propto \frac{v}{T} e^{1/T}.?? \quad (2.7)$$

2.4.1.2 Sliding speed

In the thermal activation regime (low temperature) and at low speeds the friction relation follows Eq. (2.6) making friction scale logarithmically with speed. For higher speed, $v > v_c$, if only thermal effects are considered, Eq. (2.6) predicts that friction will eventually saturate and come to a plateau at $F_{\text{fric}} = F_c$. This is illustrated in Fig. 2.6 with this prediction being represented by the dotted line. However, as given away by the figure, for higher speed the model will enter an athermal regime where the thermal effects are negligible compared to other contributions [34](32). In the athermal regime the damping term $m\mu\dot{x}$ will dominate yielding $F_{\text{fric}} \propto v$. The athermal regime is often observed in reduced models if the system is overdamped or at high speeds. This concept is also interesting in connection to MD simulations where the accessible speeds often fall into the athermal regime [41]. It is unclear how this affects real physical systems for which there exist more dissipation channels than just a single viscous term [42]. For the thermal drift regime at higher temperatures the linear relation $F_{\text{fric}} \propto v$ is predicted for low speed as well by ??.

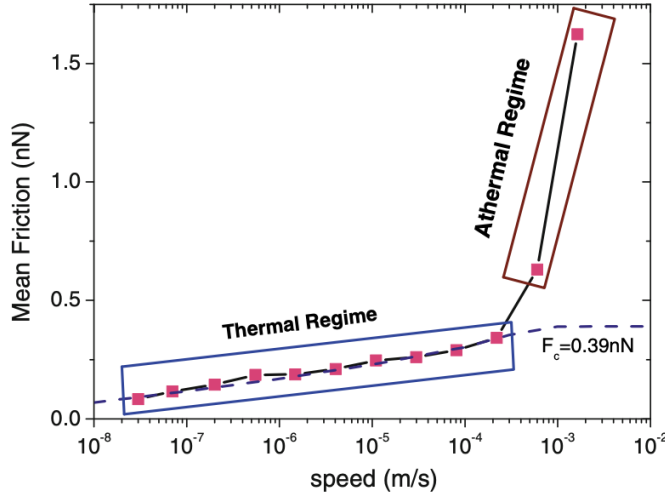


Fig. 6 Speed dependence of friction illustrating two different regimes. In the thermal regime, there is a logarithmic scaling of friction with speed, and in the athermal regime the friction is governed by the damping term such that $F \propto v$. The friction plateau ($F_c = 0.39$ nN) predicted by thermal activation is identified by the dashed line. Other model parameters: $m = 10^{-12}$ kg, $U = 0.6$ eV, $T = 300$ K, $v = 4 \times 10^3$ nm/s, $\mu = 2\sqrt{k/m}$, $a = 0.288$ nm

Figure 2.6: Temporary figure from [34]

2.4.1.3 Tip mass

The mass of the tip affects the dynamics due to a change of inertia, which changes the attempt rate f_0 . A smaller inertia leads to a larger attempt rate and vice versa. Effectively, this will affect the transition point for the temperature and speed regimes described in the previous. A smaller inertia, giving a larger attempt rate, will cause an earlier transition (i.e. at lower temperature) to the thermal drift regime, and result in a later speed saturation such that it transitions to the athermal regime at higher speed.

2.4.1.4 Friction Regimes: Smooth Sliding, Single Slip, and Multiple Slip

Stick-slip motion is a crucial instability mechanism associated with high energy dissipation and high friction. Thus, controlling the transition between smooth sliding and stick-slip is considered key to control friction. We can divide the frictional stick-slip behaviour into three regimes: 1) Smooth sliding, where the tip slides smoothly on the substrate. 2) Single slip, where the tip sticks at one potential well before jumping one lattice spacing to the next. 3) Multiple slip, where the tip jumps more than one lattice spacing for a slip event. The underlying mechanisms behind these regimes can be understood through a static and a dynamic contribution.

To understand the static mechanism we consider a quasistatic process for which temperature, speed and damping can be neglected and where we must have $\partial(V)/\partial x = 0$. This simplifies Eq. (2.3) to

$$\frac{\pi U_0}{a} \sin\left(\frac{2\pi x}{a}\right) \frac{2\pi}{a} = K(vt - x). \quad (2.8)$$

The friction regime is determined by the number of solutions x to Eq. (2.8). Only one solution corresponds to smooth sliding, two solutions to a single slip and so on. It turns out that the regimes can be defined by the parameter $\eta = 2\pi^2 U_0 / a^2 K$ [43, 44] yielding transitions at $\eta = 1, 4.6, 7.79, 10.95, \dots$, such that $\eta \leq 1$ corresponds to smooth sliding, $1 < \eta \leq 4.6$ to a single slip and so on. These static derivation lays out the fundamental probabilities for being in one of the regimes stick-slip regimes. Notice that increasing the spring constant K (stiff spring) will decrease the possibilities for stick-slip behaviour. This also agrees with Bonelli [Talk about this](#).

Considering the dynamics on top, one finds that damping, speed and temperature will affect this probability. A high damping, equivalent of a high transfer of kinetic energy to heat, will result in less energy available for the slip events. This will make multiple slip less likely. By a similar argument, we find that increasing the speed will contribute to more kinetic energy which will increase the likelihood of multiple slips. Finally, temperature will contribute to earlier slips, due to thermal activation, such that less potential energy can be accumulated and it will result in fewer multiple slips. The effects of damping, speed and temperature is illustrated for the force traces in Fig. 2.7

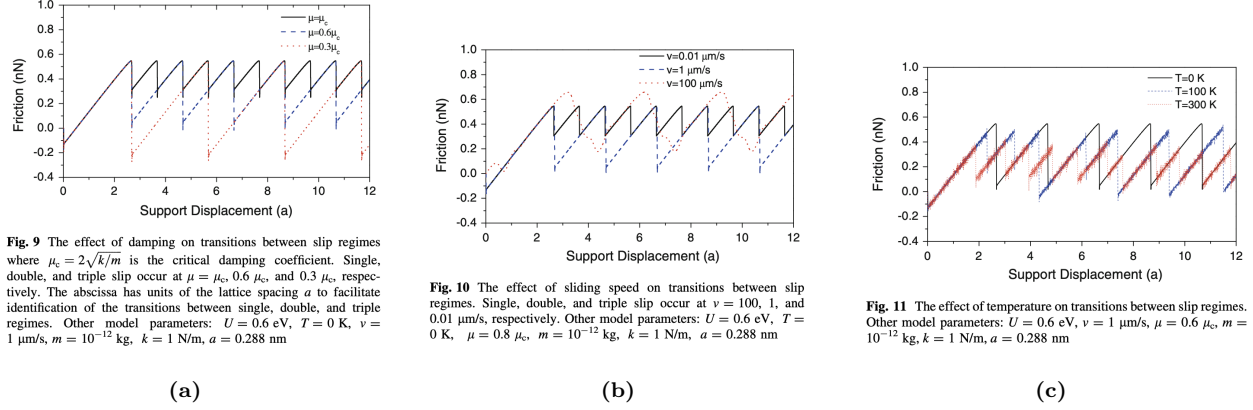


Fig. 9 The effect of damping on transitions between slip regimes where $\mu_c = 2\sqrt{k/m}$ is the critical damping coefficient. Single, double, and triple slip occur at $\mu = \mu_c$, $0.6\mu_c$, and $0.3\mu_c$, respectively. The abscissa has units of the lattice spacing a to facilitate identification of the transitions between single, double, and triple regimes. Other model parameters: $U = 0.6 \text{ eV}$, $T = 0 \text{ K}$, $v = 1 \mu\text{m/s}$, $m = 10^{-12} \text{ kg}$, $k = 1 \text{ N/m}$, $a = 0.288 \text{ nm}$

Fig. 10 The effect of sliding speed on transitions between slip regimes. Single, double, and triple slip occur at $v = 100$, 1 , and $0.01 \mu\text{m/s}$, respectively. Other model parameters: $U = 0.6 \text{ eV}$, $T = 0 \text{ K}$, $\mu = 0.8\mu_c$, $m = 10^{-12} \text{ kg}$, $k = 1 \text{ N/m}$, $a = 0.288 \text{ nm}$

Fig. 11 The effect of temperature on transitions between slip regimes. Other model parameters: $U = 0.6 \text{ eV}$, $v = 1 \mu\text{m/s}$, $\mu = 0.6\mu_c$, $m = 10^{-12} \text{ kg}$, $k = 1 \text{ N/m}$, $a = 0.288 \text{ nm}$

Figure 2.7: Temporary figure from [34]

2.4.2 Frenkel-Kontorova

The Frenkel-Kontorova (FK) model [45] extends the PT model by considering a chain of atoms in contrast to just a single particle (tip). This extension is useful for understanding the importance of the alignment between the atoms and the substrate, the so-called *commensurability*.

The standard (FK) model consists of a 1D chain of N classical particles of equal mass, representing atoms, interacting via harmonic forces and moving in a sinusoidal potential as sketched in Fig. 2.8 [15]. The hamiltonian is

$$H = \sum_{i=1}^N \left[\frac{p_i^2}{2m} + \frac{1}{2}K(x_{i+1} - x_i - a_c)^2 + \frac{1}{2}U_0 \cos\left(\frac{2\pi x_i}{a_b}\right) \right], \quad (2.9)$$

where the atoms are labelled sequentially $i = 1, \dots, N$. The first term $p_i^2/2m$ represents the kinetic energy with momentum p_i and mass m . Often the effects of inertia are neglected, referred to as the static FK model, while the inclusion in Eq. (2.9) is known as the dynamic FK model [46]. The next term describes the harmonic interaction with elastic constant K , nearest neighbour distance $\Delta x = x_{i+1} - x_i$ and corresponding nearest neighbour equilibrium distance a_c . The final term represents the periodic corrugation potential, with amplitude U_0 and period a_b . By comparison to the potential used in the PT model Eq. (2.3), the only difference is the introduction of a harmonic coupling between particles in the chain as opposed to the moving body, and that we have not yet specified any force incentivizing sliding. Different boundary choices can be made where both free ends and periodic conditions give similar results. The choice of fixed ends however makes the chain incapable of sliding.

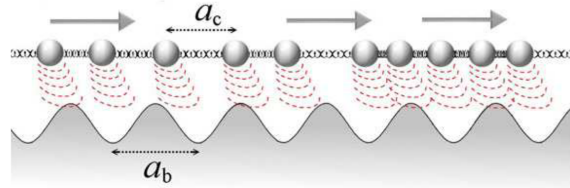


Figure 1. A sketch of the FK model, showing the two competing lengths: the average interparticle spacing and the lattice periodicity of the substrate.

Figure 2.8: Temporary figure from [15]

To probe static friction one can apply an external adiabatically increasing force until sliding accours. This corresponds to the static FK model, and it turns out that the sliding properties are entirely governed by its topological excitations referred to as so-called *kinks* and *antikinks*

2.4.2.1 Commensurability

We can subdivide the frictional behaviour in terms of commensurability, that is, how well the spacing of the atoms match the periodic substrate potential. We describe this by the length ratio $\theta = a_b/a_c = N/M$ where M denotes the number of minemas in the potential (within the length of the chain). A rational number for θ means that we can achieve a perfect alignment between the atoms in the chain and the potential minemas, without stretching the chain, corresponding to a *commensurate* case. If θ is irrational the chain and substrate cannot fully align without some stretching of the chain, and we denote this as being *incommensurate*.

We begin with the simplest commensurate case of $\theta = 1$ where the spacing of the atoms matches perfectly with the substrate potential periodicity, i.e. $a_c = a_b$, $N = M$. The ground state (GS) is the configuration where each atom is aligned with one of the substrate minema. By adding an extra atom to the chain we would effectively shift over some of the atoms, out of this ideal state, giving rise to a kink excitation. This leads to the case where two atoms will have to “share” the same potential corrugation as sketched in Fig. 2.10. On the other hand, removing an atom from the chain results in an antikink excitation where one potential corrugation will be left “atomless”. In order to reach a local minimum the kink (antikink) will expand in space over a finite length such that the chain undertakes a local compression (expansion). Notice that for low ratios of θ , fewer atoms than minema, the chain will not be able to fill each corrugation well in any case, meaning that commensurability can instead be thought of as whether the atoms are forced to deviate, by a lattice spacing, from the spacing otherwise dictated by the spring forces inbetween. When applying a tangential force to the chain it is much easier for an excitation to move along the chain than it is for the non-excited atoms since the activation energy ϵ_{PN} for a kink/antikink displacement is systematically smaller (often much smaller) than the potential barrier U_0 . Thus, the motion of kinks (antikinks), i.e. the displacement of extra atoms (atom vacancies), is represententing the fundamental mechanism for mass transport. These displacements are responsible for the mobility, diffusivity and conductivity within this model.

In the zero temperature commensurable case with an adiabatical increase in force, all atoms would be put into an accelerating motion as soon as the potential barrier energy is present. However, just as discussed for the PT model, thermal activations will excite the system at an earlier stage resulting in kink-antikink pairs traveling down the chain. For a chain of finite length these often accrour at the end of the chain running in opposite direction. This cascade of kink-antikink exications is shown in Fig. 2.9. Notice, that for the 2D case, where an island (or flake) is deposited on a surface, we generally also expect the sliding to be initiated by kink-antikink pairs at the boundaries.

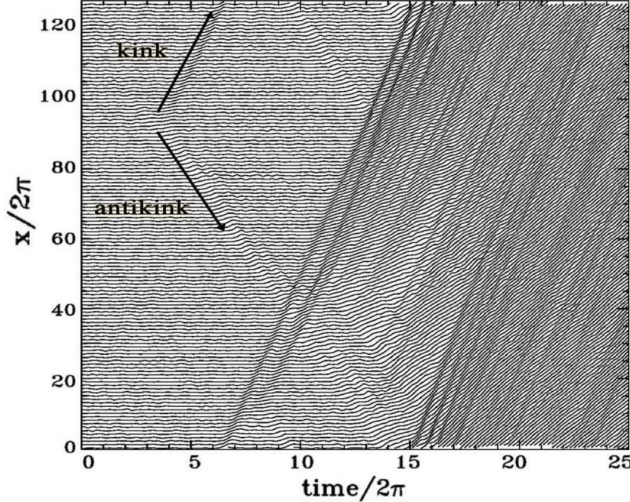


Figure 2. Time dependence of the atomic trajectories for the fully matched ($\theta = 1$) FK model at the (low-temperature) onset of depinning. Motion starts with the nucleation of a kink-antikink pair. The kink and the antikink depart in opposite directions cross the periodic boundary conditions, and collide quasielastically. A second kink-antikink pair forms in the wake of the initial kink. Further kink-antikink pairs are generated, with an avalanche-like increase of the kink-antikink concentration, eventually leading to a sliding state. Adapted from Ref. [21], Copyright (1997) by The American Physical Society.

Figure 2.9: [Temporary] figure from [15]

For the case of incommensurability, i.e. $\theta = a_b/a_c$ is irrational, the GS is characterized by a sort of “staircase” deformation. That is, the chain will exhibit regular periods of regions where the chain is slightly compressed (expanded) to match the substrate potential, separated by kinks (antikinks), where the increased stress is eventually released.



Figure 2.10: [Temporary] figure from [urlhttp://www.iop.kiev.ua/~obraun/myreprints/surveyfk.pdf](http://www.iop.kiev.ua/~obraun/myreprints/surveyfk.pdf) p. 14. Incommensurable case ($\theta = ?$) where atoms sit slightly closer than otherwise dictated by the substrate potential for which this regularly result in a kink here seen as the presence of two atoms closely together in one of the potential corrugations.

The incommensurable FK model contains a critical elastic constant K_c , such that for $K > K_c$ the static friction F_s drops to zero, making the chain able to initiate a slide at no energy cost, while the low-velocity kinetic friction is dramatically reduced. This can be explained by the fact that the displacement occurring in the incommensurable case will yield just as many atoms climbing up a corrugation as there are atoms climbing down. For a big (infinite) chain this will exactly balance the forces making it non-resistant to sliding. Generally, incommensurability guarantees that the total energy (at $T = 0$) is independent of the relative position to the potential. However, when sliding freely, a single atom will eventually occupy a maximum of the potential, and thus when increasing the potential magnitude U_0 or softening the chain stiffness, lowering K , the possibility to occupy such a maximum disappears. This marks the so-called Aubry transition, at the critical elastic constant $K = K_c(U_0, \theta)$, where the chain goes from a free sliding to a *pinned* state with a nonzero static friction. K_c is a discontinuous function of the ratio θ , due to the reliance on irrational numbers for incommensurability. The minimal value $K_c \simeq 1.0291926$ in units $[2U_0(\pi/a_b)^2]$ is achieved for the golden-mean ratio $\theta = (1 + \sqrt{5})/2$.

Notice that the pinning is provided despite translational invariance due to the inaccessibility to move past the energy barrier which act as a dynamical constraint. The Aubry transition can be investigated as a first-order phase transition for which power laws can be defined for the order parameter, but this is beyond the scope of this thesis.

The phenomena of non-pinned configurations is named *superlubricity* in tribological context. Despite the misleading name this refers to the case where the static friction is zero while the kinetic friction is nonzero but reduced. For the case of a 2D sheet it is possible to alter the commensurability, not only by changing the lattice spacing through material choices, but also by changing the orientation of the sheet relative to the substrate. Dienwiebel et al. [47] have shown that the kinetic friction, for a graphene flake sliding over a graphite surface (multiple layers of graphene), exhibits extremely low friction at certain orientations as shown in Fig. 2.11. Here we clearly see that friction changes as a function of orientation angles with only two spikes of considerable friction force. This relates back to the concept of frictional regimes introduced through the simpler PT model, where the change in orientation affects the effective substrate potential. Merely from the static consideration, we found that lowering the potential amplitude U_0 will decrease the parameter $\eta = 2\pi^2 U_0/a^2 K$ shifting away from the regime of multiple slips towards smooth sliding associated with low friction. Such transitions will also be affected by the shape of the potential and corresponding 2D effects of the sliding path [34].

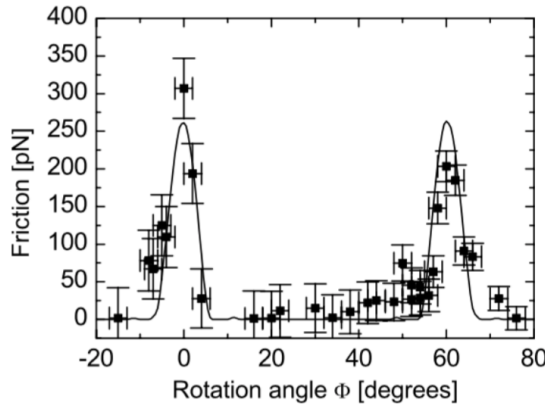


Fig. 6. Average friction force versus rotation angle Φ of the graphite sample around an axis normal to the sample surface. Two narrow peaks of high friction are observed at 0° and 61° , respectively. Between these peaks a wide angular range with ultra-low friction, close the detection limit of the instrument, is found. The first peak has a maximum friction force of 306 ± 40 pN, and the second peak has a maximum of 203 ± 20 pN. The curve through the data points shows results from a Tomlinson model for a symmetric 96-atom graphite flake sliding over the graphite surface (for details about the calculation see [39]).

Figure 2.11: [Temporary] figure from [47] showing superlubricity for incommensurable orientations between graphene and graphite. [temporary]

2.4.2.2 Velocity resonance

While many of the same arguments used for the PT model regarding velocity dependence for friction can be made for the FK model, the addition of multiple atoms introduces the possibility of resonance. In the FK model the kinetic friction is primarily attributed to resonance between the sliding induced vibrations and phonon modes in the chain [46]. The specific dynamics is found to be highly model and dimension specific, and even for the 1D case this is rather complex. However, we make a simplified analysis of the 1D rigid chain case to showcase the reasoning behind the phenomena.

When all atoms are sliding rigidly with center of mass velocity v_{CM} the atoms will pass the potential maxima with the so-called *washboard frequency* $\Omega = 2\pi v_{CM}/ab$. For a weak coupling between the chain and the potential we can use the zero potential case as an approximation for which the known dispersion relation for the 1D

harmonic chain is given [48, p. 92]

$$\omega_k = \sqrt{\frac{4K}{m}} \left| \sin\left(\frac{k}{2}\right) \right|,$$

where ω_k is the phonon frequency and $k = 2\pi i/N$ the wavenumber with $i \in [N/2, N/2)$. Resonance will occur when the washboard frequency Ω is close to the frequency of the phonon modes ω_q in the chain with wavenumber $q = 2\pi a_c/a_b = 2\pi\theta^{-1}$ or its harmonics nq for $n = 1, 2, 3, \dots$ [49]. Thus, we can approximate the resonance center of mass speed as

$$\begin{aligned} n\Omega &\sim \omega_{nq} \\ n\frac{2\pi v_{CM}}{a_b} &\sim \sqrt{\frac{4K}{m}} \left| \sin\left(\frac{2n\pi\theta^{-1}}{2}\right) \right| \\ v_{CM} &\sim \frac{\sin(n\pi\theta^{-1})}{n\pi} \sqrt{\frac{Ka_b^2}{m}}. \end{aligned}$$

When the chain slides with a velocity around resonance speed, the washboard frequency can excite acoustic phonons which will dissipate to other phonon modes as well. At zero temperature, the energy will transform back and forth between internal degrees of freedom and center of mass movement of the chain. Without any dissipation mechanism this is actually theorized to speed up the translational decay [46]. However, as soon as we add a dissipation channel through the substrate, energy will dissipate from the chain to the substrate degrees of freedom. This suggests that certain sliding speeds will exhibit relatively high kinetic friction while others will be subject to relative low kinetic friction. Simulations of concentric nanotubes in relative motion (telescopic sliding) supports this idea as it has revealed the occurrence of certain velocities at which the friction is enhanced, corresponding to the washboard frequency of the system [15], where the friction response was observed to be highly non-linear as the resonance velocities were approached.

The analysis of the phonon dynamics is highly simplified here, and a numerical study of the FK by Norell et al. [46] showed that the behaviour was highly dependent on model parameter choices, but that the friction generally increased with velocity and temperature. Here the latter observation differs qualitative from that of the PT model.

2.4.3 Frenkel-Kontorova-Tomlinson

A final extension of the atomic models worth mentioning here is the Frenkel-Kontorova-Tomlinson (FKT) model [50], which introduces a harmonic coupling of the sliding atom chain to the driving moving body, effectively combining PT and FK (see Fig. 2.3). This introduces more degrees of freedom to the model based on the intention of getting a more realistic connection between the moving body and the chain. modelling of a broad contact point. Dong et al. carried out a numerical analysis using the 1D FKT model investigating the effect of chain length. They observed that the friction increased linearly with number of atoms in the chain on a long range, but certain lattice mismatch resulted in local non-linear relationship as shown in Sec. 2.4.3. Similar, taking the FKT model to 2D they were able to achieve a similar sensitivity to commensurability as observed experimentally by [47] (shown in Fig. 2.11) with the numerical result shown in Sec. 2.4.3. Besides a recreation of the commensurability effect they also observed increasing friction with an increasing flake size. Combined, the 1D and 2D results supports the idea of an increasing friction with contact size although it might showcase non-linear behaviour depending on commensurability.

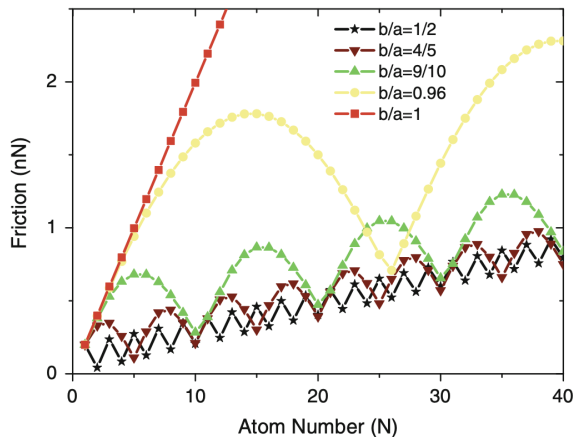


Fig. 21 Friction variation with the tip size N for different lattice mismatch b/a . $k = 5 \text{ N/m}$ and $k_t = 50 \text{ N/m}$ are used to obtain these results

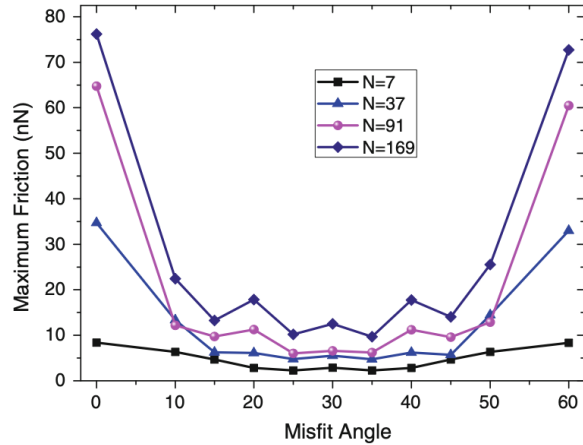


Fig. 23 The misfit angle dependence of friction with different tip sizes; $k_t = 50 \text{ N/m}$ and $k = 10 \text{ N/m}$. The $N = 7$ curve corresponds to the model illustrated in Fig. 22

(a) [Temporary] figure from [34]

(b) [Temporary] figure from [34]

2.4.4 Shortcomings of atomic models

To-DO: Shortcomings of PT-based reduced-models

- Assumes a rigid substrate with a simplified potential shape.
- Energy dissipation is added through a viscous term $-m\mu\dot{x}$ being the only dissipation channel available. Does not capture a more complex real life electron and phonon dissipation. Taking phonon dissipation as an example there are many vibrational modes ($3N$). This will effect the thermal activation derivation.
- The moving body is simplified as constant moving rigid body, while in fact this will also be subject to a more complex dynamic behavior.

2.4.5 Experimental procedures

Experimentally, the study of nanoscale friction is challenging due to the low forces on the scale of nano-newtons along with difficulties of mapping the nano-scale topography of the sample. In opposition to numerical simulations, which provides full transparency regarding atomic-scale structures, sampling of forces, velocities and temperature, the experimental results are limited by the state-of-the-art experimental methods. In order to compare numerical and experimental results it is useful to address the most common experimental.

2.4.5.1 Scanning Probe Microscopy

Scanning probe microscopy (SPM) includes a variety of experimental methods which is used to examine surfaces with atomic resolution [51, pp. 6-27]. This was originally developed for surface topography imaging, but today it plays a crucial role in nanoscale science as it is used for probe-sampling regarding tribological, electronic, magnetic, biological and chemical character. The family of methods involving the measurement of forces is generally referred to as *scanning force microscopies* (SFM) or for friction purposes *friction force microscopes* (FFM).

One such method arose from the *atomic force microscope* AFM, which consists of a sharp micro-fabricated tip attached to a cantilever force sensor, usually with a sensitivity below 1 nN all the way down to pN. The force is measured by recording the bending of the cantilever, either as a change in electrical conduction or more commonly, by a light beam reflected from the back of the cantilever into a photodetector [1, p. 183]. By adjusting the tip-sample height to keep a constant normal force while scanning across the surface this can be used to produce a surface topography map. By tapping the material (dynamic force microscopy) with sinusoidally

vibrated tip the effects from friction and other disturbing forces can be minimized in order to produce an even clearer image (include example, preferable showing the surface structure of graphene). However, when scanning perpendicularly to the cantilever axis, one is also able to measure the frictional force as torsion of the cantilever. By having four quadrants in the photodetector (as shown in figure Fig. 2.13), one can simultaneously measure the normal force and friction force as the probes scans accross the surface.

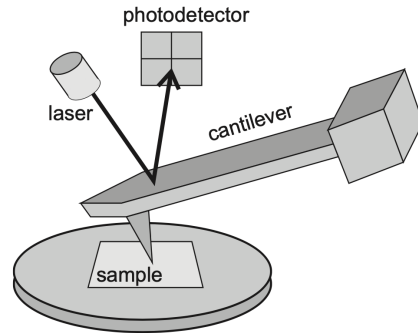


Figure 17.1 Schematic diagram of a beam-deflection atomic force microscope.

Figure 2.13: [Temporary figure from [1, p. 184]

AFM can also be used to drag a nanoflake accross the substrate as done by Dienwiebel et al. [47], where a graphene flake was attached to a FFM tip and dragged accross graphite. Notice that this makes the normal loading concentrated to a single point on the flake rather than achieving an evenly distributed load.

2.4.5.2 Surface Force Apparatus

The Surface force apparatus SFA is based on two curved molecularly smooth surfaces brought into contact [1, p. 188]. The sample is placed in between the two surfaces as surfaces as lubricant film for which the friction properties can be studied by applying a tangential force to the surfaces.

2.5 Expected frictional properties of graphene

Several studies have investigated the frictional behaviour of graphene by varying different parameters such as normal force, sliding velocity, temperature, commensurability and graphene thickness [52]. In general, we find three types of relevant systems being studied: 1) An FFM type setup where the graphene, either resting on a substrate or suspended, is probed by an AFM tip scanning across the surface. 2) SFA approach with the graphene “sandwiched” in between two substrate layers moving relative to each other using the graphene as a solid lubricant. 3) A graphene flake sliding on a substrate, either being dragged by an AFM tip or by more complex arrangements in numerical simulations. Considering that even the sharpest AFM tip will effectively put multiple atoms in contact with the test sample, all methods relates to a nanoscale contact involving graphene but differs on contact area. However, the FFM type suggest a basis in asperity theory as we expect it to deform with increasing load, while the latter two is more aligned with the PT type models and our system our interest which is an atomic flat sheet on a flat substrate. Having said that, we consider all three types with the purpose of gaining a more comprehensive insight. The relevant studies considered in the following are listed in Table 2.1 for convenience.

Table 2.1: Update multirow line span after completing the table...

System	Type	Year	Researcher	Materials	Key words
FFM	Exp.	2007 [53]	Zhao et al.	Si ₃ N ₄ tip on graphite.	Temperature dependence
		2015 [54]	G. Paolicelli et al.	Si tip, graphene on SiO ₂ and Ni(111) substrate	Layers, load, shear strength
	Both	2019 [55]	Zhang et al.	Monolayer graphene	Straining sheet
		2019 [56]	Vazirisereshk et al.	Graphene, MoS ₂ and Graphene/MoS ₂ heterostructure	Low friction?
	Num.	2015 [57]	Yoon et al.	Si tip, graphene on SiO ₂	Stick-slip: tip size, scan angle, layer thickness, substrate flexibility
		2016 [58]	Li et al.	Si tip, graphene on a-Si substrate	Increasing layers
	SFA	2011 [59]	Wijn et al.	Graphene flakes between graphite	Rotational dynamics, superlubricity, temperature
		2012 [22]	H. J. Kim and D. E. Kim.	Carbon sheet	Corrugated nano-structured surfaces
Flake	Exp.	2005 [47]	Dienwiebel et al.	Graphene on graphite	Commensurability, superlubricity
		2013 [60]	Feng et al.	Graphene on graphite	Free sliding (relevant?)
	Num.	2009 [61]	Bonelli et al.	Graphene on graphite	Tight-binding, commensurability, load, flake size
		2012 [62]	Reguzzoni et al.	Graphene on graphite	Graphite thickness
		2014 [63]	Liu et al.	Graphene on graphite	Thickness, deformations, high speed
		2018 [64]	P. Zhu and Li	Graphene on gold	Flake size, commensurability
		2019 [65]	Zhang et al.	Graphene on diamond	Temperature, sliding angle, friction coefficient

One of the earliest tribological simulations of graphene was carried out by Bonelli et al. [61] in 2009 using a tight-binding method (excluding thermal excitations) to simulate a graphene flake on an infinite graphene sheet [52]. They implemented a FKT-like setup where each atom in the flake is coupled horizontally to a rigid support by elastic springs. They recovered the stick-slip behaviour, which is also observed in FFM setups both experimentally [53, 55] and numerically [58, 64], and they found an agreement with the qualitative observation that soft springs allow for a clean stick-slip motion while hard springs inhibit it ($\lesssim 40$ N/m). In AFM and SFA experiments, the stick-slip motion tends to transition into smooth sliding when the speed exceeds $\sim 1\ \mu\text{s}$ while in MD modelling the same transition is observed in the $\sim 1\ \text{m/s}$ region [15]. This 6 order of magnitude discrepancy has been largely discussed in connection to simplifying assumptions in MD simulations.

Bonelli et al. [61] also found that commensurability, through orientation of the flake and the direction of sliding, had a great impact on the frictional behaviour which generally aligns with the predictions of the FK and FKT models. They confirmed qualitatively the experimental observation of superlubricity for certain incommensurable orientations as shown experimentally by Dienwiebel et al. [47] and further supported by experimental measurements of interaction energies by Feng et al. [60]. This commensurability importance is also reported for MD simulations [59, 64, 65]. Bonelli et al. found the friction force and coefficient to be one order of magnitude higher than that of the experimental results which they attribute to the details of the numerical modelling. Generally the experimental coefficients between graphite and most materials lies in the range 0.08-0.18 [47] and while Dienwiebel et al. [47] reported a wide range of frictional forces all the way from $28 \pm 16\ \text{pN}$ to $453 \pm 16\ \text{pN}$ in a load range $\sim [-10, 20]\ \text{nN}$ the change in friction with applied load was as low as 0.05-0.4 % (coef. of 0.0005-0.004). This indicates an almost independent relationship between friction and load which they attributed to the lack of change in contact area.

Furthermore, Bonelli et al. [61] found friction to decrease with flake size which is mainly attributed to the idea that boundary atoms are dominant in increasing friction, but also due to the fact that the coupling to the support made for a decreased rotational freedom as size increases, which could then be attributed to a forced path decreasing the tendency of stick-slip behaviour. This disagrees with the FK and FKT model which predicts the reverse, an increase in friction with increasing size, but this might be a shortage to the simplicity of the reduced-models. However, the decreasing friction with increasing flake size is also found for graphene on gold MD simulation [64]. This can however be attributed to commensurability as a numerical MD study of monolayer islands of krypton on copper by Reguzzoni and Righi [66] reports that the effective commensurability increase drastically below a critical flake radius on the order of 10 Å. In a numerical study by Varini et al. [67], based on Kr islands adsorbed on Pb(111), this is further elaborated as they found that finite size effects are especially important for static friction as a pinning barrier rise from the edge (preventing otherwise superlubricity due to incommensurability). They reported a relationship $F_s \sim A^{\gamma_s}$ not only sublinear $\gamma_s < 1$ but also sublinear with respect to the island perimeter $P \propto A^{1/2}$ by having $\gamma_s = 0.25$ for a hexagonal edge and $\gamma_s = 0.37$ when circular, indicating that only a subset of the edge is responsible for the pinning effect. This aligns with the general change in friction found by [64] for different flake geometries (square, triangle, circle). Additionally, Varini et al. also found the edge pinning effect to decrease with increasing temperature as the edge energy barriers are reduced. Bringing this all together, the main picture forming is that flake size, which we can consider as contact area, is affecting friction through a commensurability mechanism. If the flake is constrained in some way we might not observe the same dependence. While flake size nor contact area is easily measured in experimental FFM Mo et al. [19] found that $F_{\text{fric}} \propto A$ where A is the real contact area defined by atoms within chemical range.

Evolution effects, or so-called friction strengthening, are also observed, meaning that the friction force increases during the initial stick-slip cycles. This is observed experimentally by Zhang et al. [55] and numerically by Li et al. [58]. However, this is only found when having the graphene sheet resting on a substrate [55] opposed to a suspended sheet, and it was found to diminish when increasing number of graphene layers stacked (graphite) [58]. In general, the friction was found to decrease with increasing number of layers which is also supported by the findings in [57] but disagree with [62]?? Zhang et al. [55] additionally found that straining a suspended stretch, modulating the flexibility which consequently changes the local pinning capability of the contact interface and lowers the dynamic friction. Another surface manipulating study was performed by H. J. Kim and D. E. Kim. [22] where the investigated the effects of corrugated nano-structured surfaces which altered the contact area and structural stiffness resulting in both increased and slightly decreased friction under certain load ranges. These studies highlight the importance of surface structure and mechanical conditions.

TO-DO: Negative friction coefficients

The dependency on friction of normal load turns out to be a complex matter and has proven to be highly system dependent. As already mentioned, asperity theory mainly points to a sublinear relationship between friction and load, while the PT models points to a dependence through the change of the effective substrate potential leading to a commensurability effect. Experimentally rather different trends have been observed, although the majority agree on an increasing friction with increasing load [1, p. 200]. For the graphene flake Dienwiebel et al. [47] found a seemingly non-dependent relationship while FFM study by G. Paolicelli et al. [54] found a great fit with the sublinear predictions of Maugis-Dugdale theory ($F_f \propto (F_N - F_{N,0})^{2/3}$). Here the discrepancy might lie in the difference between a spherical tip indenting the graphene sheet (matching asperity theory) as opposed to atomic flatness of the graphene/graphite sheets in contact making for a constant contact area. However, numerical studies with graphene in contact with graphite still find both sublinear [61] and linear [65] load dependencies.

The dependency of velocity is generally found to increase logarithmically with velocity in experimental AFM studies [1, p. 201] which match the low velocity regime of the PT type models. At higher velocities thermally activated processes are less important and friction becomes independent of velocity according to the continuation of the Eq. (2.6) without entering the athermal regime related to the PT model which is attributed to a numerical damping effect. The saturation of the velocity dependency has been observed numerically for Si tips and diamond, graphite and amorphous carbon surfaces with scan velocities above $1 \mu\text{s}$ [68]. Guerra et al. [69] studying gold clusters on graphite using MD simulations found a viscous friction response, friction proportional to sliding velocity, in both low and high speed domains. However, thermal effects reversed: at low speed (diffusive) friction decreased with increased temperature while at high speed (ballistic) speed friction increases with temperature. In the MD simulations the crossover from ballistic to diffusive occurred between 10 and 1 m/s.

For the temperature the general experimental trend is an decreasing friction with increasing temperature as found by Zhao et al. [53] in a series of AFM graphene on graphite experiments with $F_{\text{fric}} \propto \exp(1/T)$.

This agrees with the thermal drift regime of the PT type models even though the temperature range used in the study does not match the range of this regime according to the PT model. Wijn et al. [59] find that friction commensurability can be lost at higher temperature (above 200K) were the found a power law behaviour $F_k \propto T^{-1.13 \pm 0.04}$. Numerically, Zhang et al. [65] found that friction increased with temperature, using a velocity of 10 m/s. Considering the findings of [69] related to MD this qualitative different dependence might be due the to low speed diffisive behvaiour as opposed to high speed ballistic behaviour in MD simulations.

A summary of the expectations is given in Table 2.2.

Table 2.2: Summary

Stick slip	Generally we expect to observe periodic stick-slip motion with a period matching the lattice constant(s) involved [19]. This is however inhibited for high stiffness of the spring coupling to a driving support and at large sliding velocity.
Static friction	The static friciton is highly related to the presence of stick-slip motion. The static friction is most pronounced for commensurable configurations and will decrease drastically for incommensurability. However, further reducton of static friction is expected for an increasing flake size and increasing temperature.
Commensurability	Both static and dynamic friction is expected to be highly sensitive to commensurability, through lattice spacing, orientation of the flake relative to the substrate and by the path of sliding along the substrate. By changing the spring stiffness of the coupled driving support we expect to get a response in commensurability due to a change in translational freedom.
Friction evolution (Friction strengthening)	Friction evolution is found to be present in mono layer graphene resting on a substrate, and thus we expect this to be present in our simulaiton setup as well.
Negative coef	TO-DO
Normal load	Generally an increasing friction force is expected with increasing load. Both non-dependent, sublinear and linear relationship can be expected here.
Velocity	Generally an increasing friction force is expected with increased sliding velocity. Experimental results suggest that kinetic friction goes as $F_k \propto \ln(v)$, with the expectation that friction become independent of velocity at “high” velocities above 1 μ /s. Numerically a viscous $F_k \propto v$ is expected for all velocity ranges.
Temperature	Experimentally and numerically friction is expected to decrease with friction in a power law or exponential manner. However, for high velocity ranges, according to a ballistic regime, which might coincide with the capabilities of MD, the friction is predicted to increase with temperature.
Contact area	For our system we do not expect any contact area changes during load, however an increasing number of atoms in contact is expected to increase friction.

2.6 Research questions

Part II

Simulations

Chapter 3

Pilot study

Having defined our system, we carry out an initial study of the numerical approach. This includes an analysis of how to define and measure the frictional properties of interest, and an investigation of the main parameters governing the numerical solutions. From this point of view we decide on suitable parameters for the remaining study. Particularly, we investigate the frictional behaviour under the variation of load and stretch for a selected set of configurations which serves as a baseline for later comparison and an assessment of the prospects of Kirigami modifications for friction.

3.1 Friction simulation parameters

The MD simulation is governed by a small set of parameters, some which are related directly to the numerical aspects of the simulation and other related to the physical conditions we are simulating. Thus, we differentiate between the two main categories: 1) *Physical*, parameters which alter the physical conditions of the “numerical experiment” and are expected to effect the frictional behaviour. 2) *Numerical*, parameters which are related more closely to the numerical procedure itself, expected to influence the simulation dynamics, which should be chosen to ensure the most stable results. For the purpose of creating the machine learning dataset most of these parameters will be kept constant with only a subset of the physical parameters being varied. The parameters are summarized in Table 3.1 where the grey shaded area marks the parameters, Configuration, stretch and load, which we will vary for the dataset. Due to the great number of parameters it is unreasonable to make an exhaustive search of all parameters before deciding on the final settings. Instead, we take a basis in the parameters used in similar studies **SOURCES** and adjust them as we carry out the initial analysis of the simulation results. Thus, we start at values most representative for other similar simulations and adjust according to the stability of the results and the computation time. Since we are going to introduce a lot of complexity to the system, through the cut and stretch deformation, we are less concerned about aligning parameters for comparison. Instead of presenting the process of narrowing down the final parameters in a chronological manner, we have shown the final choice shown in Table 3.1 which we will discuss throughout the following presentation of the pilot study. Notice, that the values in Table 3.1 serve as default values which are used when nothing else is stated.

Table 3.1: Parameters of the numerical MD simulation for measuring friction. The values correspond to the final choice used for the dataset. The shaded area denote the parameters varied in the ML dataset.

Category	Parameter	Value	Description
Physical	T	300 K	Temperature.
	v_{slide}	20 m/s	Sliding speed for the sheet translation.
	K	inf	Spring constant for the coupling between the virtual atom and the sheet pull blocks.
	Scan direction	$(x, y) = (0, 1)$ (zigzag direction)	The direction for which we translate the sheet.
	Sheet configuration	Contiguous	Binary mapping describing which atoms are removed (0) and which is still present (1) in the graphene sheet.
	Stretch amount	0% - rupture	The relative stretch of the sheet.
	F_N	[0.1, 10] nN	Applied normal force to the pull blocks.
Numerical	dt	1 fs	Integration timestep.
	t_R	15 ps	Relaxtion time before strething.
	Pauses	5 ps	Relaxtion pauses after stretch, and during the normal load phase (before translating the sheet).
	Stretch Speed	0.01 ps^{-1}	The rate of stretching for the sheet.
	Slide distance	400 Å	How far to translate the sheet.
	Sheet size	$130.029 \times 163.219 \text{ \AA}$	Spatial 2D size of the sheet.
	Pull block size	$2 \times 130.029 \times 15.183 \text{ \AA}$	Spatial 2D size of the pull blocks.

3.2 Force traces

We begin by assessing the friction force traces, i.e. force vs. time curves, for a single friction simulation using the default parameters shown in ?? for a non-cut sheet with no stretch applied and a normal load of 1 nN.

3.2.1 Force oscillations

We evaluate the friction force as the force acting on the sheet from the substrate. We consider initially the force component F_{\parallel} parallel to the drag direction as plotted in Fig. 3.1. We use a sample rate of $10 \text{ ps}^{-1} = 100 \text{ timesteps}^{-1}$ for which each sample is the mean value of the preceding 100 timesteps. We observe immediately that the data carriers oscillations on different time scales matching our general expectations for sliding involving periodic surfaces. By applying a savgol filter to the data with a polyorder of 5 and window length of 150 timesteps (corresponding to a sliding distance of 3 Å or a time window of 15 ps) we can qualitatively point out at least two different frequencies of oscillation. During the first 10 Å of sliding, seen in Fig. 3.1a, we see roughly three waves on the savgol filter corresponding to a relative high frequency, while for the duration of 100 Å of sliding, seen in Fig. 3.1b, the same savgol filter reveals a lower frequency on top, creating the visual pattern of a wavepacket. The data does not indicate clear signs of stick-slip behaviour as otherwise found in other studies, e.g. by Zhu and Li [64] for graphene on gold, who saw a more typical saw tooth shape in the force trace. Beside the difference in substrate material, using gold instead of silicon, they used a lower sliding speed of 10 m/s and a soft spring of $K = 10 \text{ N/m}$. By adopting those parameters we get a slightly different force trace behaviour as shown in Fig. 3.1c and Fig. 3.1d. This change breaks the symmetry in the force oscillations, but still does not produce any significant discontinuities in the trace. By keeping the spring constant $K = 10 \text{ N/m}$ and lowering the sliding speed further down to 1 m/s we are able to demonstrate a proper stick-slip behaviour as shown in Fig. 3.1e and Fig. 3.1f. Considering all three simulations we might classify the results from the default settings, $K = \text{inf}$, $v = 20 \text{ m/s}$, as smooth sliding, $K = 10 \text{ N/m}$, $v = 10 \text{ m/s}$, as a transition phase with possible occasional slipping, and $K = 10 \text{ N/m}$, $v = 1 \text{ m/s}$ as certain stick-slip behaviour.

Refer a bit to theory on this one

However, the low sliding speed comes with a high computational cost which is the reason that we choose a sliding speed of 20 m/s. The choice of an infinite spring constant is related to the stability of the measurements as discussed later [make reference](#).

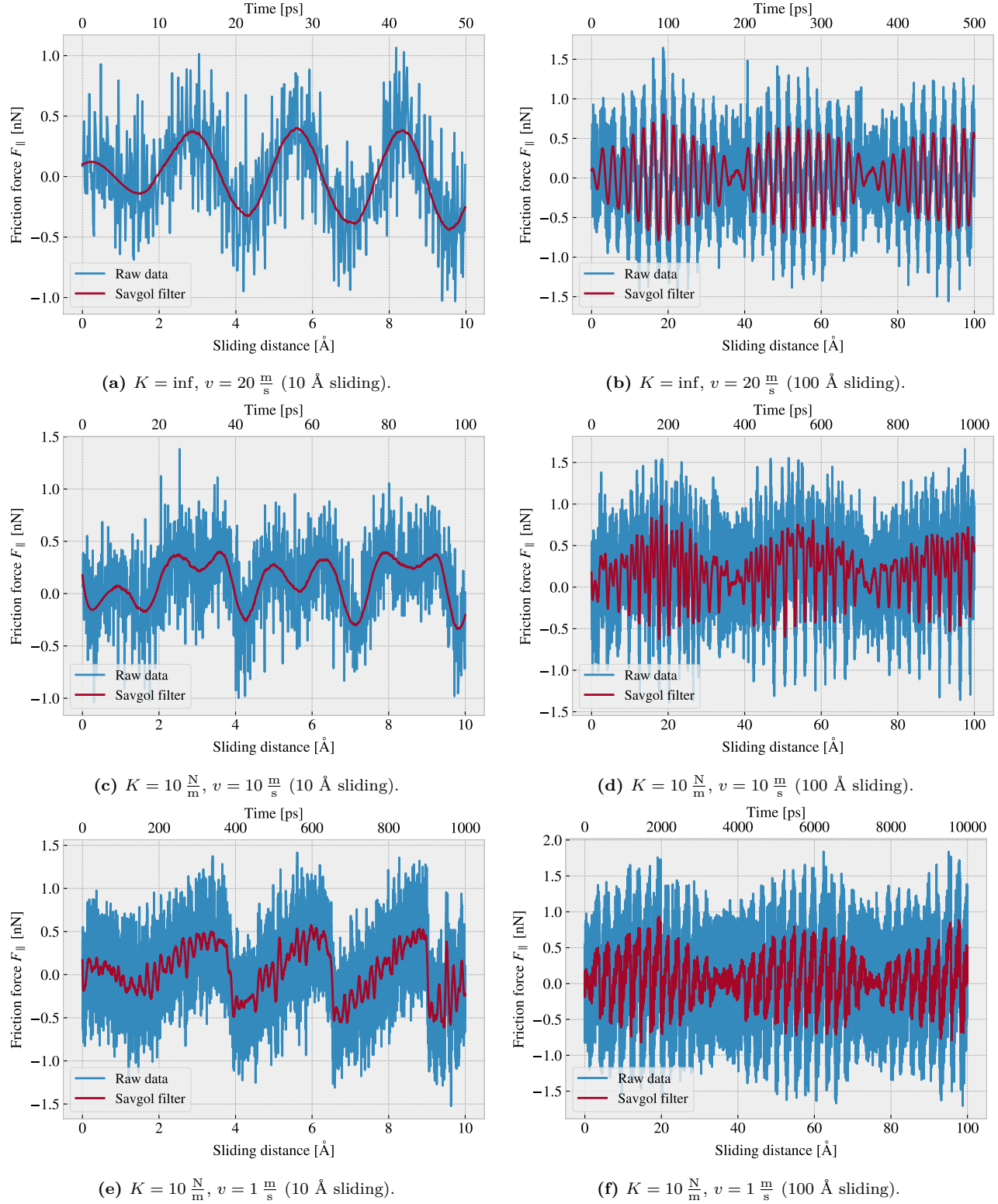


Figure 3.1: Force traces of the friction force F_{\parallel} with respect to the drag direction between acting from the substrate on the full sheet and substrate. The force traces is plotted against the sliding distance (lower x-axis) and the corresponding sliding time (upper x-axis). The sliding distance is measured by displacement of the virtual atom tethering the sheet. The red line represents a savgol filter with window polyorder 5 and window length of 150 timesteps (corresponding to a sliding distance of 3 \AA or a time window of 15 ps). Each row, (a,b), (c,d), (e,f), represents a different choice of the spring constant K and sliding speed v , while the columns show the same result for two different time scales. The default settings are represented in figure (a) and (b).

By performing a Fourier Transform on the data, using the default parameters, we can quantify the leading frequencies observed in figure Fig. 3.1a and Fig. 3.1b. The Fourier transform is shown in Fig. 3.2a, and by plotting the two most dominant frequencies $f_1 = 0.0074 \text{ ps}^{-1}$ and $f_2 = 0.0079 \text{ ps}^{-1}$ as a sine sum, $\sin(2\pi f_1) + \sin(2\pi f_2)$, we find a qualitatively convincing fit to the observed wavepacket shape as seen in Fig. 3.2b. We can convert the frequencies according to that of a wavepacket. By using the trigonometric identity

$$\begin{aligned}\sin(a+b) &= \sin(a)\cos(b) + \cos(a)\sin(b), \\ \sin(a-b) &= \sin(a)\cos(b) - \cos(a)\sin(b),\end{aligned}$$

and decomposing the frequencies as $f_1 = a - b$, $f_2 = a + b$, we can rewrite the sine sum as the sinusoidal product

$$\begin{aligned}\sin(2\pi f_1) + \sin(2\pi f_2) &= \sin(2\pi(a-b)) + \sin(2\pi(a+b)) \\ &= \sin(2\pi a)\cos(2\pi b) + \cancel{\cos(2\pi a)\sin(2\pi b)} + \sin(2\pi a)\cos(2\pi b) - \cancel{\cos(2\pi a)\sin(2\pi b)} \\ &= 2\sin(2\pi a)\cos(2\pi b),\end{aligned}$$

with

$$\begin{aligned}a &= \frac{f_1 + f_2}{2} = 0.0763 \pm 0.0005 \text{ ps}^{-1}, & b &= \frac{f_2 - f_1}{2} = 0.0028 \pm 0.0005 \text{ ps}^{-1}, \\ &= 0.381 \pm 0.003 \text{ \AA}^{-1}, & &= 0.014 \pm 0.003 \text{ \AA}^{-1},\end{aligned}$$

where the latter frequency is denoted with respect to the sliding distance. This makes us recognize the high oscillation frequency as a and the low frequency as b . The faster one has a period of $T_a = 2.62 \pm 0.02 \text{ \AA}^3$ which corresponds well with the magnitude of the lattice spacing and especially that of graphene at 2.46 \AA as expected theoretically. The longer period $T_b = 71 \pm 15 \text{ \AA}^{-1}$ is not obviously explained. We noticed a similar long period oscillation for all three cases, Fig. 3.1b, Fig. 3.1d and Fig. 3.1f, regarding stick-slip behaviour, and thus we do not believe that this is directly related. The initial build up in friction force is reminiscent of a friction strengthening, which is often reported SOURCE, but the periodicity goes against this idea. Instead, we might attribute it to some kind of phonon resonance which could be a physical phenomenon or simply a feature of our MD modelling.

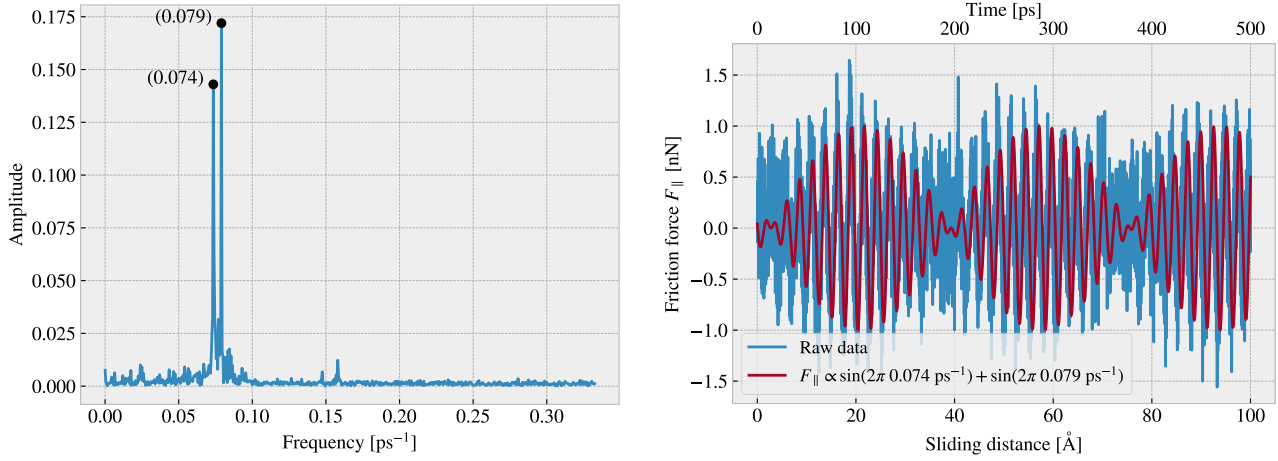


Figure 3.2: Fourier transform analysis of the full friction force data (all 400 Å sliding distance) shown in Fig. 3.1. (a) shows the two most dominant frequency peaks. Note that no significant peaks were found in a higher frequency than included here. (b) shows a comparison between the raw data and the wavefunction corresponding to the two peaks in figure (a).

³The uncertainty Δy is calculated as $\Delta y = \left| \frac{\partial y}{\partial x} \Delta x \right|$ for uncertainty Δx and $y(x)$

3.2.2 Decompositions

In the previous analysis we have looked only at the friction force for the full sheet, including the rigid pull blocks, and with respect to the drag direction. We found this way of measuring the friction force to be the most intuitive and reliable, but we will present the underlying arguments for this choice in the following.

Due to the fact that we are only applying cuts to the inner sheet, and not the pull blocks, it might seem more natural to only consider the friction on that part. If the desired frictional properties can be achieved by altering the inner sheet one can argue that any opposing effects from the pull blocks can be mitigated by simply scaling the relative size between the inner sheet and the pull blocks. However, when looking at the force traces decomposed with respect to the inner sheet and pull block regions respectively, see Fig. 3.3a, we observe that the friction force arising from those parts are seemingly antisymmetric. That is, the distribution of the frictional pull from the substrate on the sheet is oscillating between the inner sheet and the pull block. Keeping in mind that normal force is only applied to the pull blocks we might take this as an intrinsic feature of the system which does not necessarily disappear by scaling of the spatial ratio between the inner sheet and pull block. Any interesting friction properties might depend on this internal distribution of forces. Hence, we hedge our bets and use the full sheet friction force as a holistic approach to avoid excluding relevant information in the measurement data.

Similar we might question the decision of only considering the frictional force projected onto the sliding direction as we are then neglecting the “side shift” induced during sliding. In Fig. 3.3b we show the decomposition in terms of force components parallel F_{\parallel} and perpendicular F_{\perp} to the sliding direction respectively. We notice that the most dominant trend appears for the parallel component. If we want to include the perpendicular component as well we would have to evaluate friction as the length of the force vector instead, but this would remove the sign of the force direction and shift the mean friction force up as we clearly see both negative and positive contributions in the parallel force trace. One option to accommodate this issue is by using the vector length for the magnitude but keeping the sign from the parallel component. However, we omit such compromises as this might make the measurement interpretation unnecessary complex, and we use only the parallel component going forward.

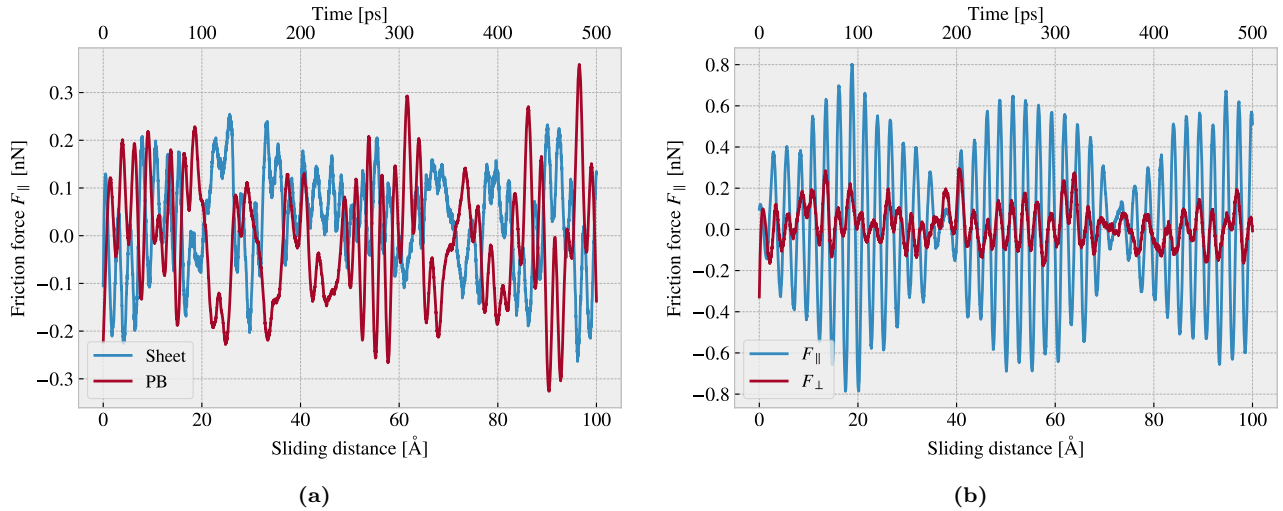


Figure 3.3: Friction force decomposition on the default parameter force trace shown in Fig. 3.1 showing only the applied savgol filters. (a) Decomposition into group inner sheet (sheet) and pull blocks (PB). (b) Decomposition into parallel (F_{\parallel}) and perpendicular (F_{\perp}) to drag sliding direction.

3.2.3 Center of mass path

From the previous observations of the force traces Fig. 3.1 we demonstrated both smooth sliding and stick-slip behaviour. Considering the force decomposition in Fig. 3.3b we know that the frictional forces in the perpendicular direction to sliding is also present. By looking at the x, y -position for the sheet Center of Mass (CM) we see a qualitatively different behaviour when reconsidering the spring constant and sliding speed investigated in Fig. 3.1 which is shown in Fig. 3.4. The default case in Fig. 3.4a shows a rather straight path forward with only a

small side motion in comparison to the cases in Fig. 3.4b and Fig. 3.4c. However, the CM accelerates and deaccelerates with a high frequency, much too high to be associated with the lattice spacing on the order of 2.46 Å (interatomic distance of 1.42 Å). One possible explanation is that the sheet and substrate constitutes an incommensurable contact for which travelling kink excitations make the atoms move in such a way that the sheet CM is incremented in small “burst”. When looking at the $K = 10 \frac{\text{N}}{\text{m}}$, $v = 10 \frac{\text{m}}{\text{s}}$ case in Fig. 3.4b we see a completely different CM path where the rapid parts aligns visually better with the force oscillations shown earlier in Fig. 3.1d. The CM accelerates forward and the deaccelerates in combination with a side motion that lead to the CM path making a loop as it slows down. Finally we have the $K = 10 \frac{\text{N}}{\text{m}}$, $v = 1 \frac{\text{m}}{\text{s}}$ in Fig. 3.4b which is confirmed to have stick-slip behaviour in Fig. 3.1f. Here the CM path shows a more chaotic movement between acceleration which also aligns visually well with the timing of the slips seen in Fig. 3.1f. The chaotic motion is not obviously connected to the stick-slip motion, but we omit a further investigation as this is not corresponding to the parameters that we will be using.

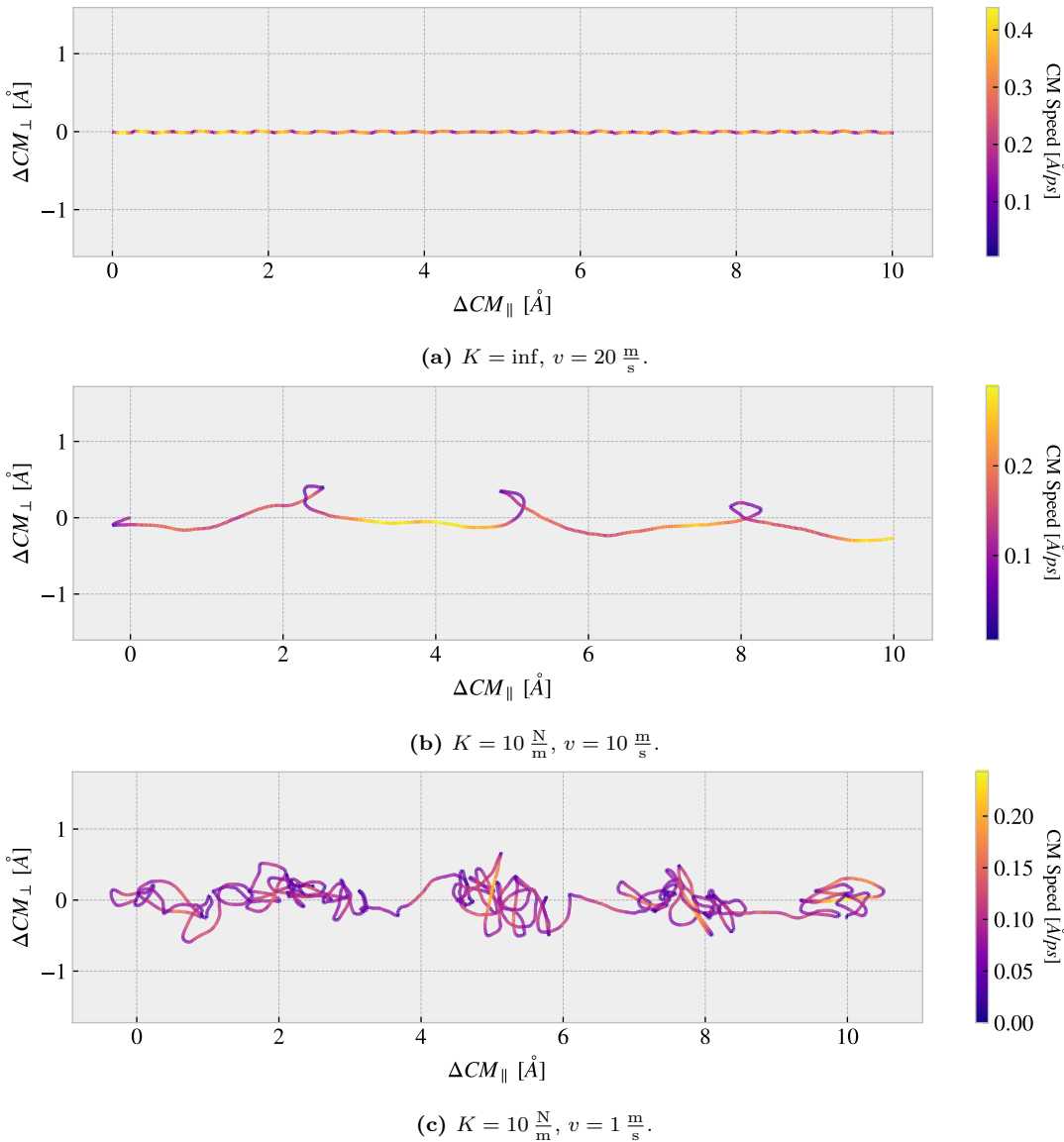


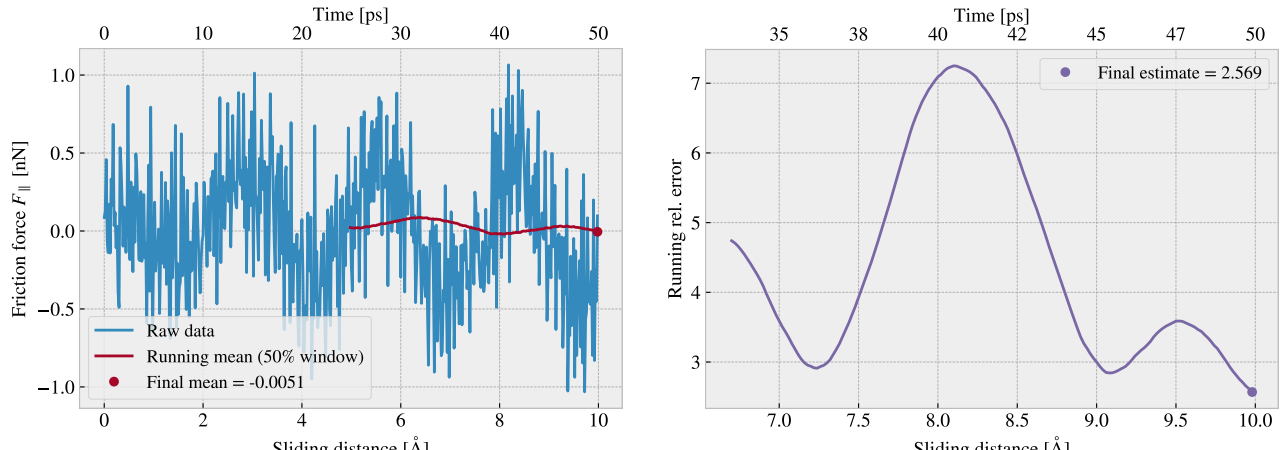
Figure 3.4: Center of Mass (CM) position relative to the start of the sliding phase in terms of the direction parallel to the sliding direction ΔCOM_{\parallel} and the axis perpendicular to the sliding direction ΔCOM_{\perp} . The colorbar denotes the absolute speed of the CM motion. Figure a-c shows different parameters used for the spring constant K and sliding speed v similar to that used in Fig. 3.1. (a) Default: $K = \infty$, $v = 20 \frac{\text{m}}{\text{s}}$. (b) $K = 10 \frac{\text{N}}{\text{m}}$, $v = 10 \frac{\text{m}}{\text{s}}$. (c) $K = 10 \frac{\text{N}}{\text{m}}$, $v = 1 \frac{\text{m}}{\text{s}}$

3.3 Defining metrics for friction

In order to evaluate the frictional properties of the sheet we aim to reduce the force trace results, addressed in section Sec. 3.2, into single metrics describing the kinetic and static friction respectively.

3.3.1 Kinetic friction

We measure kinetic friction as the mean of the friction force trace. More precisely, we take the mean value of the latter half of the dataset in order to ensure that we are sampling from a stable system. For a full sliding simulation of 400 Å we thus base our mean value on the latter 200 Å (1000 ps) of sliding. In Fig. 3.5a we have shown the force trace for the first 10 Å of sliding together with a 50% running mean window. The choice of such a short sliding distance is merely to illustrate the sampling procedure, and we see that the final mean estimate (marked with a dot) takes a negative value due to the specific cut-off of the few oscillations captured here. Nonetheless, one approach to quantify the uncertainty of the final mean estimate is to consider the variation of the running mean preceding the final mean value. The more the running mean fluctuates the more uncertainty associated with the final estimate. Only the running mean “close” to the ending should be considered, since the first part will rely on data from the beginning of the simulation. From the Fourier analyse in section Sec. 3.2.1 we found the longest significant oscillation period to be $\sim 71 \text{ \AA}^{-1}$ corresponding to $\sim 35\%$ of the running mean window which gives a window length of 200 Å when including all the data. Hence, we use the standard deviation of the final 35% of the running mean to approximate the uncertainty of the final mean value. We consider the standard deviation (std) as an estimate of the absolute error and calculate the relative error by a division of the final mean value. In Fig. 3.5b we showcase a running relative error based on the std, with a window of length 35% the mean window, in a continuation of the illustrative case of a 10 Å sliding from Fig. 3.5a. In this case we get an extremely high relative error of $\sim 257\%$, but this is desirable since the sampling period leads to an unphysical negative value which should be associated with a high uncertainty.



(a) Running mean with window length 5 Å (50% the data length). (b) Running std with window length 1.75 Å (35% the mean window length.)

Figure 3.5: Running mean (a) and running relative error (std) (b) on the friction force data from a reduced sliding distance of 10 Å. The running mean window is 50% the data length while the running std window is 35% the running mean window length. The values are plotted at the end of their respective windows such that window precedes the actual point on the graph.

When including the full dataset of 400 Å of sliding, such that the std window actually matches with the longest period of oscillations expected, we get a final relative error of $\sim 12\%$ as shown in fig Fig. 3.6. This is arguable just at the limit of an acceptable error, but as we shall see later on in Sec. 3.6 this high relative error is mainly associated with the cases of low friction. When investigating different configurations under variation of load and stretch we see a considerable lower relative error as the mean friction evaluates to higher values. One interpretation of this finding is simply that the oscillations in the running mean are to some degree independent of

the magnitude of the friction. In that case, the relative error will spike for the low friction cases, and the absolute error might be there more reliable measure, i.e. taken simple the std without dividing by the final mean value.

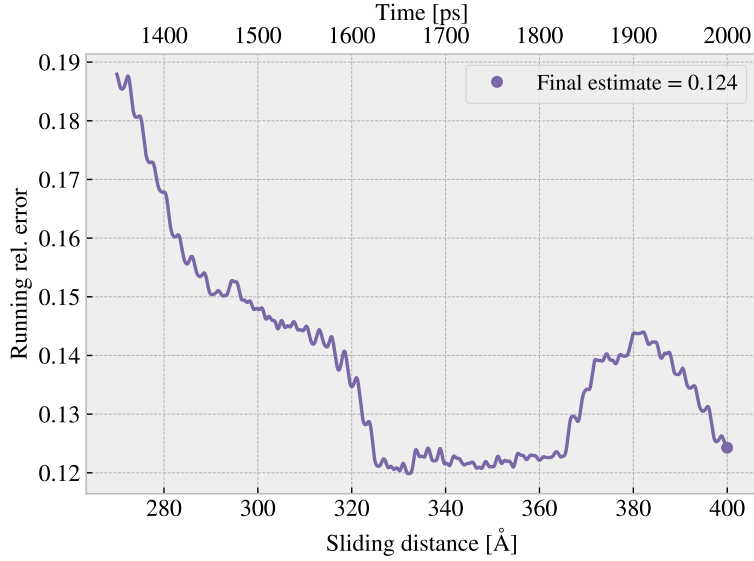


Figure 3.6: Running standard deviation (std) for a full 400 Å sliding simulation. The running std window is 70 Å (35% the running mean window of 50% the data length).

3.3.2 Static friction

The maximum value is one of the common choices for addressing static friction, even though the definition of static friction is a bit vague. When considering the force traces in Fig. 3.1 we observe that the force oscillations increase in magnitude toward a global peak at $\sim 20 \text{ \AA}$. Thus, one could be inclined to identify this peak as the maximum value associated with the static friction force. However, as we have already clarified, this steady increase in friction is a part of a slower oscillation which repeats by a period of $\sim 71 \text{ \AA}^{-1}$. By plotting the top three max values recorded during a full 400 Å simulation, for 30 logarithmically spaced load values in the range $[0.1, 100] \text{ nN}$, we observe that the global max in fact rarely fall within this first oscillation period as shown in Fig. 3.7. Only 2/30 global maxima and 4/90 top three maxima can be associated to the start of the sliding by this definition. Thus, this result suggests that our default system does not yield a static friction response in the sense of an initial increase in friction due to a depinning of the sheet from the static state **Is this probably defined in the theory section?** Some parameter changes that might increase the likelihood of seeing a significant static friction response is either extending the relaxation period, as static friction is theorized to increase logarithmically with time, or to increase the sliding force more slowly and through a soft spring tethering. As an attempt to test parts of this hypothesis we run a series of simulations with varying spring constant, $K \in [5, 200] \text{ nN}$ including also $K = \inf$, but keeping the relaxation time and sliding speed at the default values. The result is shown in Fig. 3.8. The results do not show any support of the hypothesis that a softening of the spring constant will eventually lead to the maxima occurring in the first period of sliding. We note that this might be suppressed by having a too short relaxation period or a too high sliding speed, related to the rate of which force increased initially, but due to the ambiguousness in the assessment of the static friction we will mainly concern ourselves with the kinetic friction in the remaining of this thesis.

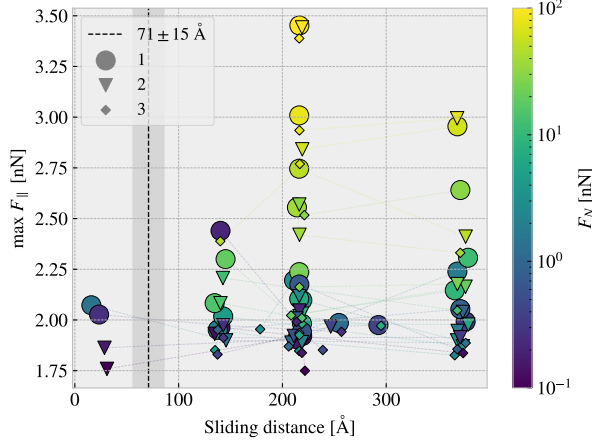


Figure 3.7: Distribution of top three max friction force peaks for 30 uniformly sampled normal forces $F_N \in [0.1, 10]$ nN. The dotted line and the grey area marks the slowest significant oscillation period found in the data and thus marking a dividing line for whether a peak falls within the “beginning” of the sliding simulation.

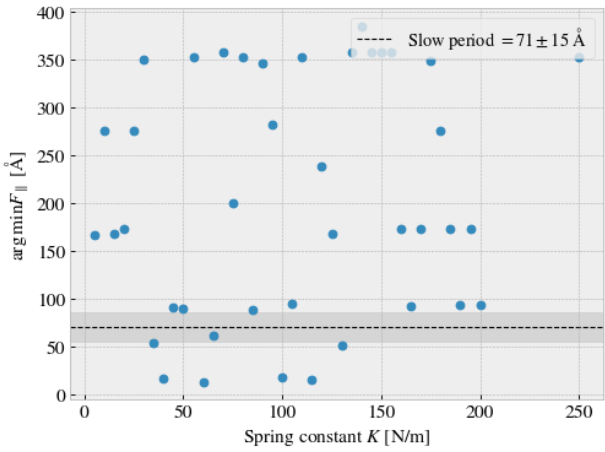


Figure 3.8: Sliding displacement for the max friction peak to appear as a function of spring constant. Fixmove is tmp mapped to $K = 200$ here without any discontinuous lines.

3.4 Out-of-plane buckling

The out-of-plane buckling is one of the original motivations for investigating the application of Kirigami cuts in the context of friction properties. Therefor, we perform a stretch simulation, at low temperature ($T = 5$ K) without any substrate, in order to verify that we are able to reproduce an out-of-plane buckling with the intended patterns described in ???. For this investigation we include the non-cut sheet, the Tetrahedron (7, 5, 1) and the Honeycomb (2, 2, 1, 5) pattern. We quantify the out-of-plane buckling by assessing the distribution of atoms along the z-direction (perpendicular to the plane) during stretching. We calculate the minimum and maximum z-value as well as the atom count quartiles 1%, 10%, 25%, 50% (median), 75%, 90% and 99% as shown in figure Fig. 3.9. The results show significant buckling for the Tetrahedron and Honeycomb patterns in comparison to the non-cut sheet which only exhibit minor buckling of ~ 2 Å which is on the same order as the lattice spacing. Moreover, we notice that the Tetrahedron pattern buckles more in consideration to the min. and max. peaks while the remaining quantiles actually seem to be more closely spaced than for the Honeycomb. By addressing the simulation visually, using the Open Visualization Tool OVITO, we find that this can be attributed to fringes on the edge “flapping around” and thus increasing the min. and max. values.

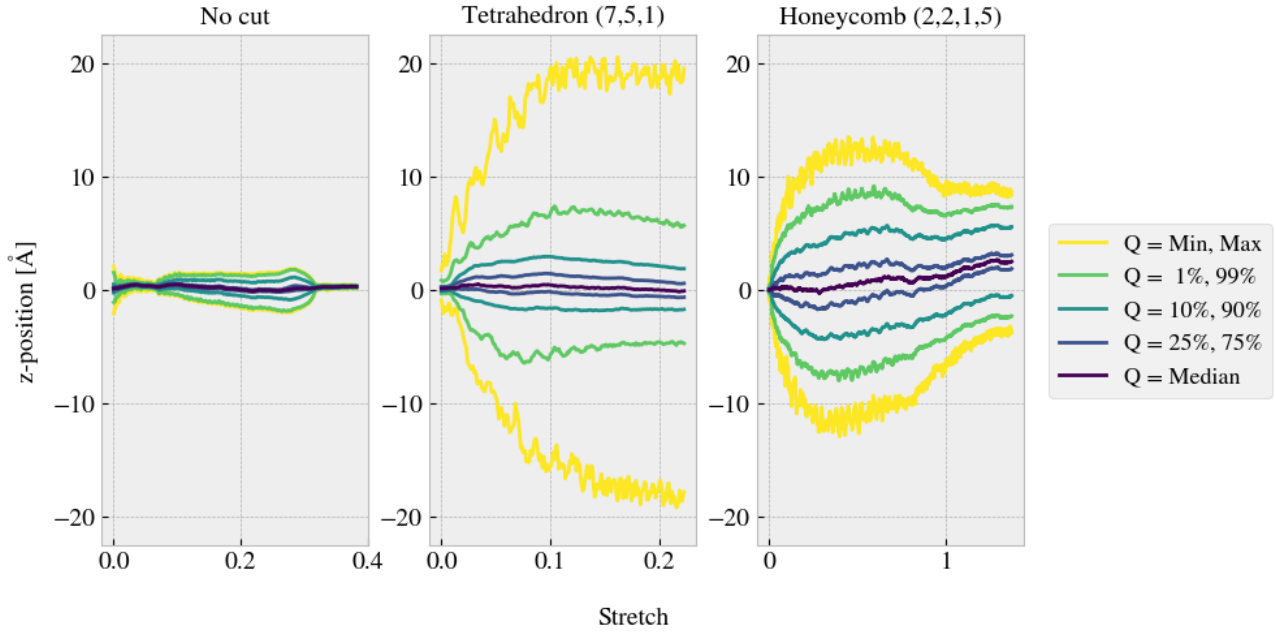


Figure 3.9: Out-of-plane buckling during stretching of the No cut, Tetrahedron (7, 5, 1) and Honeycomb (2, 2, 1, 5) sheet respectively in vacuum at low temperature $T = 5$ K. The buckling is measured by the distribution of the atom z-position (perpendicular to the sheet plane), for which the colors indicates selected quantiles. The yield strain were, reading from left to right, 0.38, 0.22 and 1.37.

Given the confirmation of out-of-plane buckling in a vacuum, as seen in Fig. 3.9, we reintroduce the substrate in order to investigate whether this effect carries over to a change in contact area. We raise the temperature to the default value of $T = 300$ K. We keep the normal force off and let the sheet stick purely by the adhesion forces between the sheet and substrate. We quantify the contact area through the relative amount of atoms in the sheet within chemical range of the substrate. The cut-off for this interaction is set to 4 Å, inspired by [58], corresponding to $\sim 120\%$ the LJ equilibrium distance. Usually the contact area is calculated as the number of contacting atoms multiplied with an associated area for each atom. However, since we are not interested in the absolute value of the actual area, but rather the relative change, we omit the multiplication factor. That is, we consider the relative number of atoms within contact range, which is proportional to the contact area, as our metric of choice. The relative contact for the three configurations (No cut, Tetrahedron (7, 5, 1) and Honeycomb (2, 2, 1, 5)) during stretching are shown in figure Fig. 3.10. The figure reveals a significant drop in contact as the sheets are stretched, which agrees qualitatively with the buckling observed without the substrate (Fig. 3.9). The Honeycomb pattern turns out to be both the most stretchable, with a rupture strain at 127% its original length, and the one with the biggest decrease in relative contact down to approximately 43%. Notice, that the relative contact is never actual 1.0 but instead maxes out at around 96% with no stretching. This is attributed to the temperature fluctuations and the choice of cut-off.

Selected frames from the simulation result are shown in appendix ?? which reveals a bit more information of how the buckling occurs. The Tetrahedron pattern deforms rather quickly and smoothly into small tetrahedron spikes, as the name suggests. While the Tetrahedron deformation appeared rather uniformly the Honeycomb pattern deformations initiate from one side first. As the sheet stretches more rows of the pattern are activated, producing the honeycomb looking shape when seen from above. As both patterns approach the rupture point the tensions lead to a small increase in the relative contact again. This agrees with the results in Fig. 3.9 where the buckling reduces slightly towards the end.

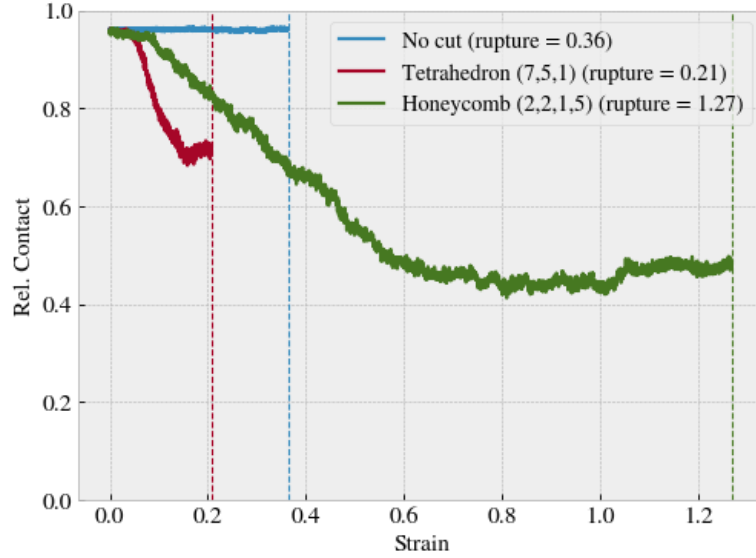


Figure 3.10: Relative contact, given as the relative number of atom in the sheet being within chemical interaction range, vs. strain of the sheet. The cut-off for the interaction range is 4 Å corresponding to $\sim 120\%$ the LJ equilibrium distance. No normal force is applied and temperature is kept at $T = 300$ K.

Compare figure Fig. 3.10 to that of figure Fig. 3.12 where multiple simulations constitute the stretch-contact curve.

3.5 Investigating main parameters

We carry out a more extensive investigation of the dependence on friction of the physical parameters temperature T , sliding speed v_{slide} and spring constant K , and the numerical parameter timestep dt . This is done partly to understand how the dependencies relate to theoretical, numerical and experimental results, and partly to understand how these parameters effects the stability of our system. We use the default parameters presented in ?? and investigate the results as we change a single parameter, one at a time. We keep the load at 1 nN. We consider the mean friction force, sampled from the latter half of the simulation as described in Sec. 3.3, representing the kinetic friction. The results are presented Fig. 3.11. We have indicated the absolute error visually, defined by the std as described in Sec. 3.3, as a shaded area which connects linearly between data points. Generally, we notice that the parameter dependencies differs between the different configurations.

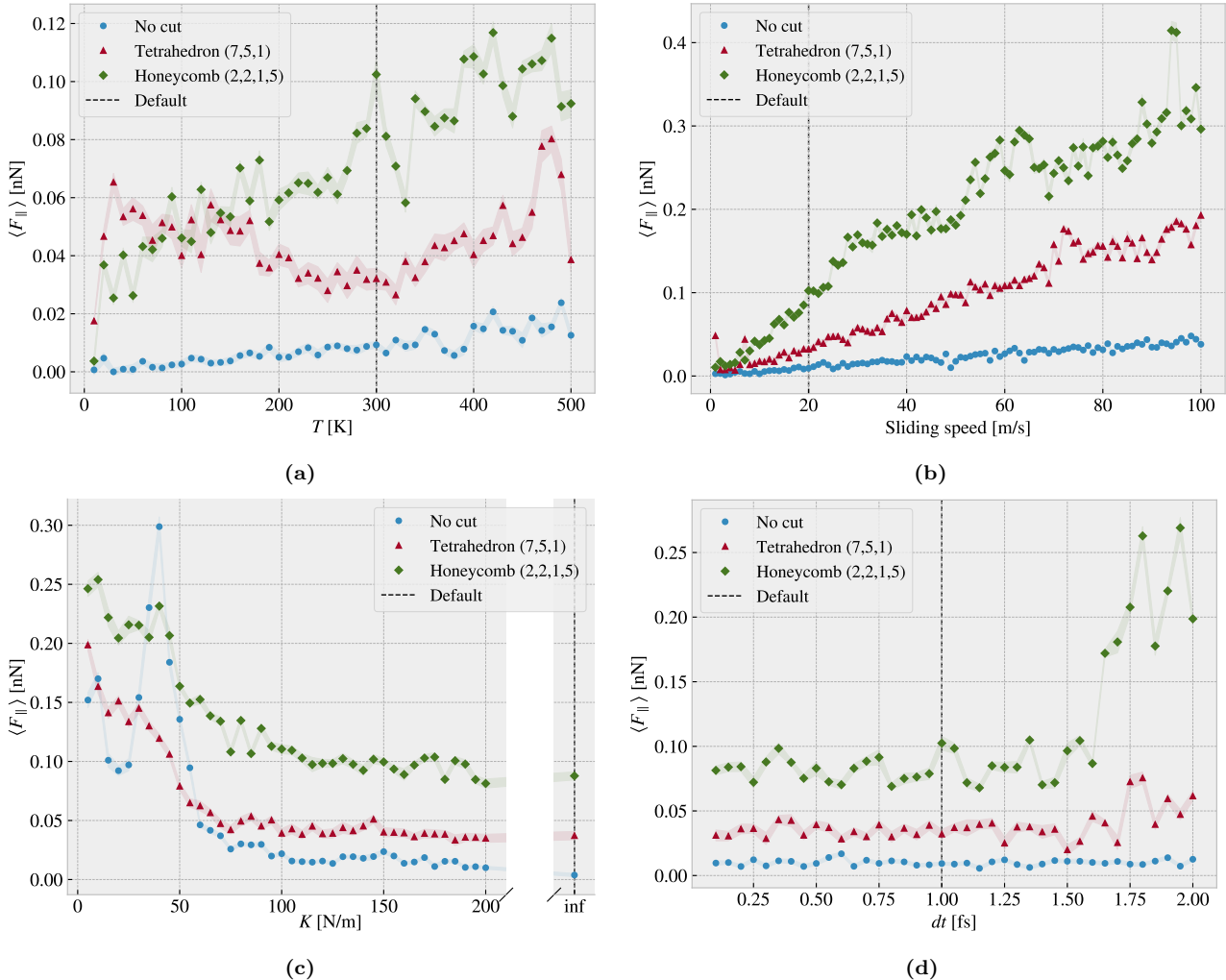


Figure 3.11: Main parameters investigation. Kinetic friction force

From the temperature investigation in Fig. 3.11a we find an increasing kinetic friction with temperature for both the non-cut sheet and the Honeycomb pattern. The Tetrahedron pattern shows both decreasing and increasing trends as it yields an initial rapid (10–30 K), followed by a more slowly decrease (30–320 K), which turns around and increases (320–480 K), and finally a rapid drop decrease again (480–500 K). Similar rapid changes are also seen from the Honeycomb pattern, although the underlying trend is seemingly increasing throughout. We notice that for the non-cut and Honeycomb sheet, which can be attributed some sort of underlying linear increase, the rate of increase is higher for the Honeycomb than the non-cut sheet. From a theoretical and experimental point of view we would expect a decrease in friction with temperature. However, an increasing trend is also observed by Zhang et al. [65] (sliding at 10 m/s) which we associates with a high sliding speed causing ballistic motion [Revisit theory on this one](#). Since the results does not indicate any plateau for which the temperature choice is more or less stable with respect to changes, we have choosen the room temperature $T = 300$ K

From the sliding speed investigation in Fig. 3.11b we generally find an increasing friction with velocity. Due to the relatively high velocities available and the effects from the thermostat, we expect a viscous friction $F_k \propto v_{\text{sliding}}$ which matches rather well with these results. However, the Tetrahedron and Honeycomb sheets seem to fall slightly into a sublinear relationship as it approaches higher velocities. Moreover, the cut sheets exhibit some local fluctuations which might be attributed to resonance effects as discussed with respect to the phonon dynamics. Our choice of sliding speed at 20 m/s mainly reflects a consideration of computational cost, but the fact that no immediate resonance fluctuations appears around this values supports the choice.

From the investigation of the spring constant parameter in Fig. 3.11c we observe a significant decrease in friction as the springs stiffens. This can be attributed to the transition from a stick-slip influenced regime to a smooth sliding regime as we saw for the force traces in Fig. 3.1. For soft springs the result is quite sensitive to the specific choice of spring constant which is especially seen for the non-cut sheet as it peaks at $K = 40 \text{ N/m}$. Thus, in order to avoid such a sensitivity we settled for the infinite stiff spring with the intention of getting more stable results in our configuration investigation.

Finally, we consider the stability of the result as we vary the simulation timestep in Fig. 3.11d. The general trend shows a stable plateau below $\sim 1.5 \text{ fs}$ for which higher values reveal arising instabilities for the cut sheets. This mainly confirms that our choice of timestep is within a reasonable range. However, we do see some fluctuations which are more significant for the cut patterns. These fluctuations can be taken as a sign of the sensitivity to randomness in our simulation. An extended study of the effect of changing the random seed for the initial velocity and thermostat could bring more insight into this matter. However, we might interpret this as an indication that the uncertainty is higher than otherwise estimated by the running mean and running std evaluation. For the Honeycomb sheet the fluctuations are on the order ± 0.017 which corresponds to a relative error of $\sim 20\%$. This number is a bit unsettling, but we take note of this as an upper limit for the error at an unstretched stage.

3.6 Load and stretch dependencies

So far, we have carried out a general analysis of the system behaviour under different parameters which lays the foundation for the remaining study. We now shift our intention to the main focus of the study which involves the friction dependence of load and stretch.

3.6.1 Pressure reference for normal load

We will consider the load range of $0.1\text{--}10 \text{ nN}$ which aligns with the general choice in other MD studies [SOURCE](#). In order to relate the magnitude of this load we provide a short calculation of the corresponding pressure. We will use the pressure underneath a stiletto heeled shoe as a high pressure reference from our macroscale world. The diameter of a stiletto heeled shoe can be less than 1 cm [70], and hence a 80 kg man⁴ standing on one stiletto heel (with all the weight on the heel) will correspond to a pressure

$$P = \frac{F}{A} = \frac{mg}{r^2\pi} = \frac{80 \text{ kg} \cdot 9.8 \frac{\text{m}}{\text{s}^2}}{\left(\frac{1 \times 10^{-2} \text{ m}}{2}\right)^2\pi} = 9.98 \text{ MPa}.$$

While this is in itself an interesting realization that is often used in introductory physics courses [71] to demonstrate the rather extreme pressure under a stiletto heel (greater than the foot of an elephant), this serves as a reasonable upperbound for human executed pressure. With a full sheet area of $\sim 21 \times 10^3 \text{ \AA}^2$ our load range of $0.1\text{--}10 \text{ nN}$ corresponds to a pressure of $0.47\text{--}47 \text{ MPa}$. Of course this pressure might be incomparable for various industrial purposes, but with no specific application in mind this serves as a decent reference point. Notice that if we consider a human foot with area 113 cm^2 [72] the pressure drops to a mere 70 kPa corresponding to only $\sim 0.01 \text{ nN}$.

3.6.2 Contact area

??

We reproduce the contact area investigation of Fig. 3.10 with the modification that the contact count is measured as an average of the latter 50% of the sliding simulation at a non-zero applied normal load. The results are shown in Fig. 3.12 with 30 attempted (some rupture) stretch (pseudo) uniformly distributed stretch between 0 and the rupture point and 3 uniform distributed normal loads in the interval $[0.1, 10] \text{ nN}$.

⁴Yes, a man can certainly wear stiletto heels.

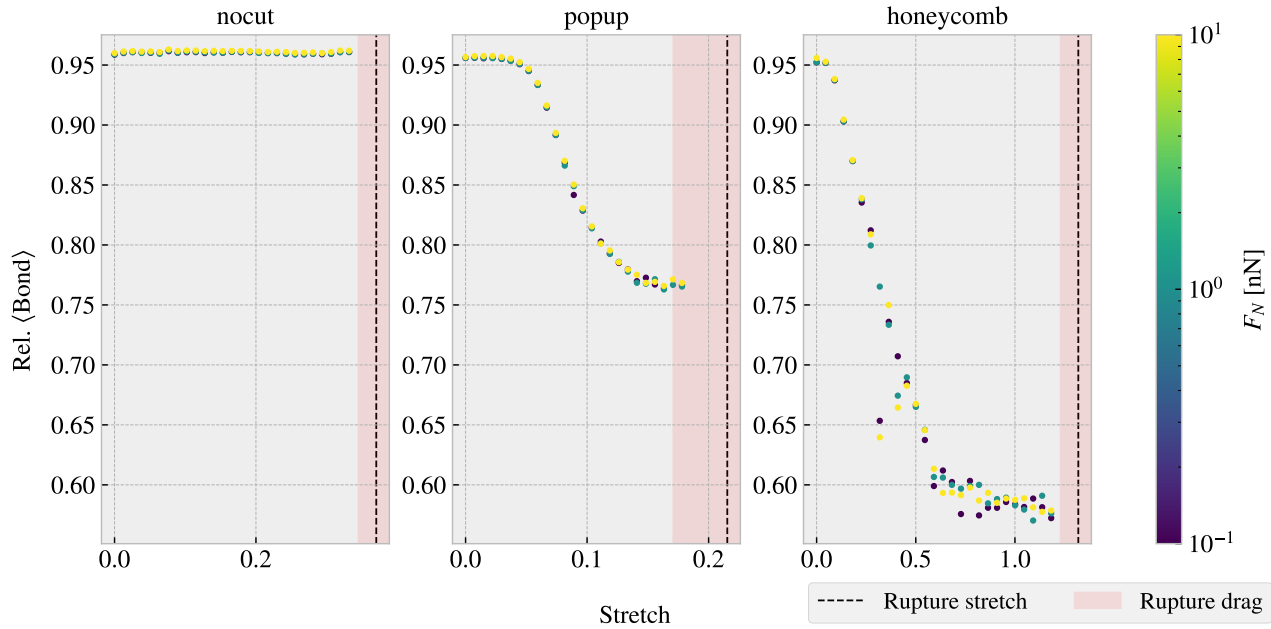


Figure 3.12: Average relative amount of bonds between the sheet and the substrate defined by the cut-off distance of 4 Å. The average is taken over the latter half of the sliding phase. The red shade denotes the stretch range where ruptures accour at certain normal loads under sliding while the black-dotted line represent the rupture point due to stretching (rupture test)

From Fig. 3.10 we observe a significant decrease in the contact due to stretching of the cut configurations in contrast to the non-cut which stays roughly constant. This is reminiscent of the non-sliding stretch vs. contact curve shown in Fig. 3.10. Given these results, theoretically one would expect the kinetic friction to decrease with stretch for the cut configurations.

3.6.3 Stretch

We make a similar analysis as done in the previous section ?? with the substitution of friction force instead of contact (The data is taken from the same simulaitons runs). The kinetic friction force (put uncertainty here even though that it is quite low?) and the max friction is shown in Fig. 3.13a and Fig. 3.13 respectively.

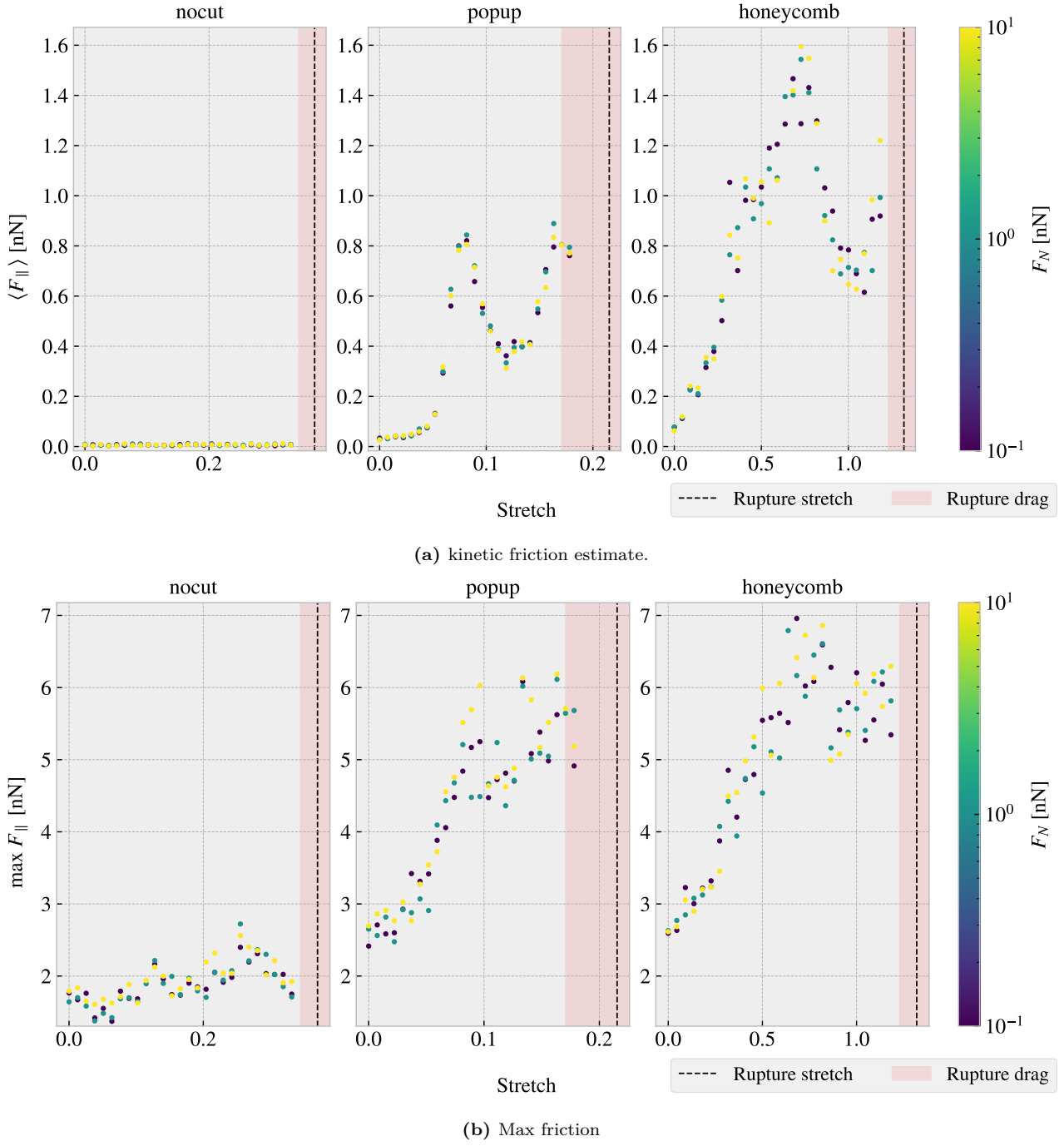


Figure 3.13: CAPTION

From Fig. 3.13a we find to our surprise that the kinetic friction increase with stretch for the cut configurations despite a simultaneous decrease in contact area as shown in figure Fig. 3.12. This suggests that the amount of chemical bonding atoms is not the dominant mechanism for the friction of this system. Instead, we might point to a mechanism more mechanical of nature associated to phonon excitations. When the cut sheet is stretched the stress (show stress maps somewhere or not necessary?) might induce a certain distribution and magnitude of point pressures to favor energy dissipation. Nonetheless, the results showcase a strong coupling between stretch and friction force, also for the max friction force, which is beyond the expectations at this stage of the study. The non-cut configuration does not show significant dependency on the stretch which reveal that this effect is only present when combining cut and stretch and not purely by stretching the sheet.

By considering the increase in kinetic friction towards the first peak we get a relative friction increase and increase vs. stretch ratios as described in Table 3.2. While the honeycomb force increase towards the first peak is approximately linear the popup exhibits seemingly exponential growth which yield a slope on the order ~ 30 nN.

Table 3.2: (stretch, kinetic friction) coordinates from Fig. 3.13a at start and the first peak respectively used to approximate the relative increase in friction force and the ratio for friction increase vs. stretch for sait range. In practice the latter ratio denotes the slope of a forced linear trend.

Configuration	Start	First peak	Relative increase	Friction force vs. stretch ratio [nN]
Popup	$\sim (0, 0.03)$	$\sim (0.082, 0.83)$	27.7	9.76
Honeycomb	$\sim (0, 0.07)$	$\sim (0.728, 1.57)$	22.4	2.06

Additionally, we notice that both the popup and honeycomb also exhibits stretch ranges where the kinetic friction force decrease with increasing stretch. Qualitatively we assign the slope to be on the same order of magnitude as those towards the first peak. This is useful for the prospect of taking advantage of this phenomena as we can essentially achieve both higher and lower friction for increasing stretch for different starting points.

3.6.4 Normal force

Main take away from this section should be that the normal force does not really change the friction much; The friction coefficient is extremely low, but I'm not sure how well the linear fits are (whether they are linear or sublinear). Not sure if I should do a linearly increasing normal force for better linear plots?

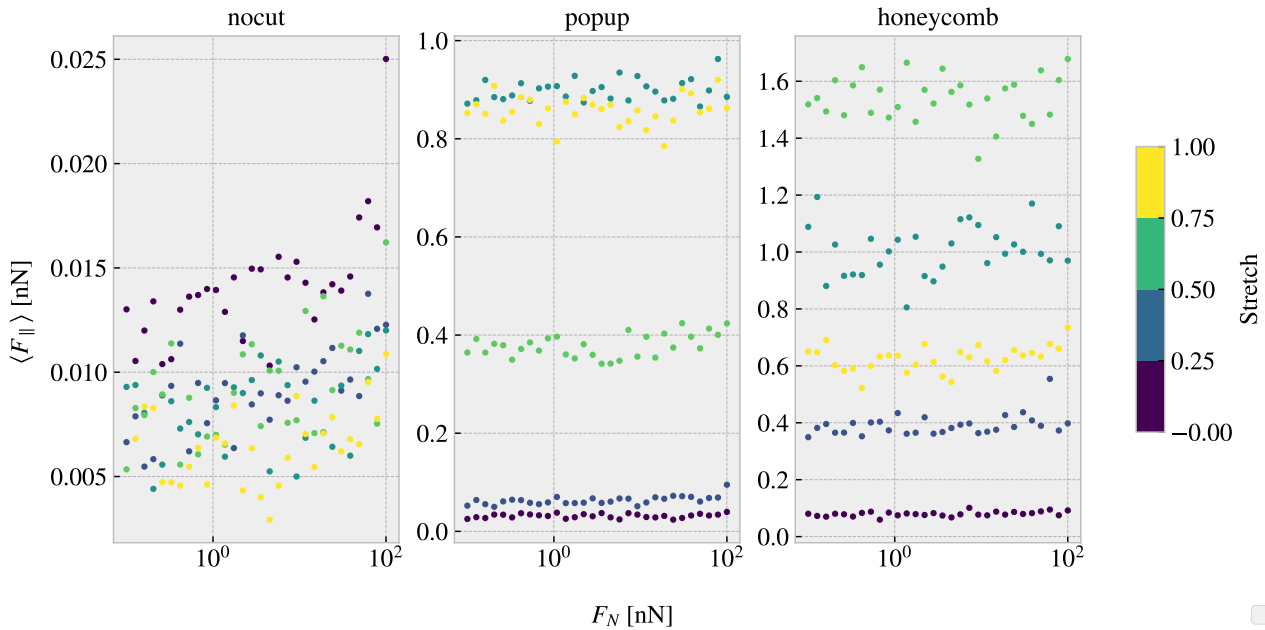


Figure 3.14: ...

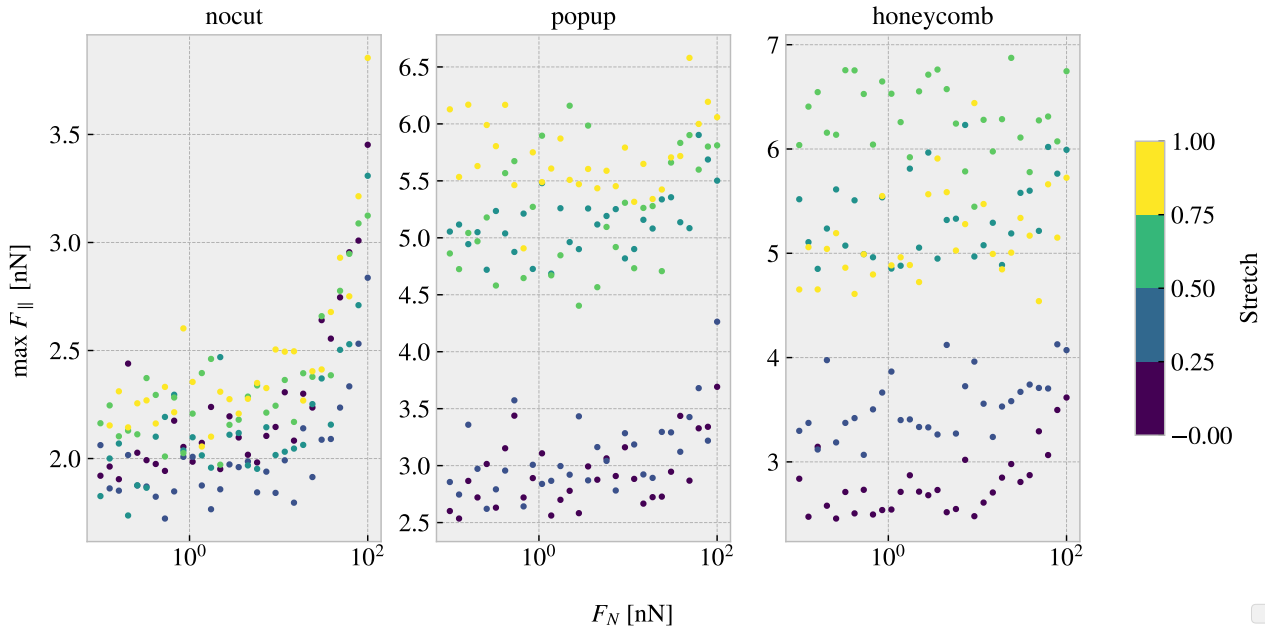


Figure 3.15: Colorbar is only fitted for the right plot (honeycomb)... this should be fixed. Should I have run a linear distribution of FN so I could plot it linear here also...?

Table 3.3: Mean friction coeff

nocut	$0.00009 \pm 1 \times 10^{-5}$	$0.00005 \pm 1 \times 10^{-5}$	$0.00004 \pm 1 \times 10^{-5}$	$0.00005 \pm 2 \times 10^{-5}$	
popup	$0.00005 \pm 3 \times 10^{-5}$	$0.00024 \pm 5 \times 10^{-5}$	$0.0002 \pm 2 \times 10^{-4}$	$0.0005 \pm 1 \times 10^{-4}$	$0.0003 \pm 2 \times 10^{-4}$
honeycomb	$0.00013 \pm 6 \times 10^{-5}$	$0.0006 \pm 3 \times 10^{-4}$	$0.0004 \pm 6 \times 10^{-4}$	$0.0007 \pm 6 \times 10^{-4}$	$0.0009 \pm 3 \times 10^{-4}$

Table 3.4: Max friciton coeff

nocut	$0.0139 \pm 9 \times 10^{-4}$	$0.0083 \pm 7 \times 10^{-4}$	$0.010 \pm 1 \times 10^{-3}$	$0.0105 \pm 9 \times 10^{-4}$	
popup	$0.007 \pm 2 \times 10^{-3}$	$0.010 \pm 2 \times 10^{-3}$	$0.007 \pm 2 \times 10^{-3}$	$0.009 \pm 3 \times 10^{-3}$	$0.006 \pm 2 \times 10^{-3}$
honeycomb	$0.010 \pm 1 \times 10^{-3}$	$0.007 \pm 2 \times 10^{-3}$	$0.007 \pm 3 \times 10^{-3}$	$0.000 \pm 3 \times 10^{-3}$	$0.004 \pm 3 \times 10^{-3}$

One theory for the low friction coefficient might dependent on the fact that the normal force is only applied on the pull blocks. Especially with the cutted sheet the tension drops such that the effecive normal force on the inner sheet is not changing very much. By this theory the friction force vs. normal force on the pull blocks should look a bit more like expected and we might make some plots of thoose to check

When looking at the graphs for the PB the max friction is visually textbook linear, while the mean friction is a bit more linear but also with negativ coefficients...

3.7 Computational cost

Talk about the computatational cost of different choices. How does computation time scale with drag speed, dt and maybe T and K as well. One could also mention scaling with system size.

Show how the number of cores per simulation scale to argue that running on just one core (maybe 4) is smart for the next step of many simulations.

Mention the trouble with GPU to show that this was considered, and in fact this was the reason for choosing the Tersoff potential over the AIREBO which is perhaps more common these days...

Appendices

Appendix A

Appendix B

Appendix C

Bibliography

- ¹E. Gnecco and E. Meyer, *Elements of friction theory and nanotribology* (Cambridge University Press, 2015).
- ²Bhusnur, “Introduction”, in *Introduction to tribology* (John Wiley & Sons, Ltd, 2013) Chap. 1, 1–?
- ³H.-J. Kim and D.-E. Kim, “Nano-scale friction: a review”, *International Journal of Precision Engineering and Manufacturing* **10**, 141–151 (2009).
- ⁴K. Holmberg and A. Erdemir, “Influence of tribology on global energy consumption, costs and emissions”, *Friction* **5**, 263–284 (2017).
- ⁵B. Bhushan, “Gecko feet: natural hairy attachment systems for smart adhesion – mechanism, modeling and development of bio-inspired materials”, in *Nanotribology and nanomechanics: an introduction* (Springer Berlin Heidelberg, Berlin, Heidelberg, 2008), pp. 1073–1134.
- ⁶P. Z. Hanakata, E. D. Cubuk, D. K. Campbell, and H. S. Park, “Accelerated search and design of stretchable graphene kirigami using machine learning”, *Phys. Rev. Lett.* **121**, 255304 (2018).
- ⁷P. Z. Hanakata, E. D. Cubuk, D. K. Campbell, and H. S. Park, “Forward and inverse design of kirigami via supervised autoencoder”, *Phys. Rev. Res.* **2**, 042006 (2020).
- ⁸L.-K. Wan, Y.-X. Xue, J.-W. Jiang, and H. S. Park, “Machine learning accelerated search of the strongest graphene/h-bn interface with designed fracture properties”, *Journal of Applied Physics* **133**, 024302 (2023).
- ⁹Y. Mao, Q. He, and X. Zhao, “Designing complex architectured materials with generative adversarial networks”, *Science Advances* **6**, eaaz4169 (2020).
- ¹⁰Z. Yang, C.-H. Yu, and M. J. Buehler, “Deep learning model to predict complex stress and strain fields in hierarchical composites”, *Science Advances* **7**, eabd7416 (2021).
- ¹¹A. E. Forte, P. Z. Hanakata, L. Jin, E. Zari, A. Zareei, M. C. Fernandes, L. Sumner, J. Alvarez, and K. Bertoldi, “Inverse design of inflatable soft membranes through machine learning”, *Advanced Functional Materials* **32**, 2111610 (2022).
- ¹²S. Chen, J. Chen, X. Zhang, Z.-Y. Li, and J. Li, “Kirigami/origami: unfolding the new regime of advanced 3D microfabrication/nanofabrication with “folding””, *Light: Science & Applications* **9**, 75 (2020).
- ¹³Z. Deng, A. Smolyanitsky, Q. Li, X.-Q. Feng, and R. J. Cannara, “Adhesion-dependent negative friction coefficient on chemically modified graphite at the nanoscale”, *Nature Materials* **11**, 1032–1037 (2012).
- ¹⁴R. W. Liefferink, B. Weber, C. Coulais, and D. Bonn, “Geometric control of sliding friction”, *Extreme Mechanics Letters* **49**, 101475 (2021).
- ¹⁵N Manini, O. M. Braun, E Tosatti, R Guerra, and A Vanossi, “Friction and nonlinear dynamics”, *Journal of Physics: Condensed Matter* **28**, 293001 (2016).
- ¹⁶B. Bhushan and A. V. Kulkarni, “Effect of normal load on microscale friction measurements”, *Thin Solid Films* **278**, 49–56 (1996).
- ¹⁷J. Gao, W. D. Luedtke, D. Gourdon, M. Ruths, J. N. Israelachvili, and U. Landman, “Frictional forces and amontons’ law: from the molecular to the macroscopic scale”, *The Journal of Physical Chemistry B* **108**, Publisher: American Chemical Society, 3410–3425 (2004).
- ¹⁸J. H. Dieterich, “Time-dependent friction in rocks”, *Journal of Geophysical Research (1896-1977)* **77**, 3690–3697 (1972).
- ¹⁹Y. Mo, K. T. Turner, and I. Szlufarska, “Friction laws at the nanoscale”, *Nature* **457**, 1116–1119 (2009).

- ²⁰G. Carbone and F. Bottiglione, “Asperity contact theories: do they predict linearity between contact area and load?”, *Journal of the Mechanics and Physics of Solids* **56**, 2555–2572 (2008).
- ²¹F. Bowden and D. Tabor, *The friction and lubrication of solids*, International series of monographs on physics vb. 1 (Clarendon Press, 2001).
- ²²H.-J. Kim and D.-E. Kim, “Molecular dynamics simulation of atomic-scale frictional behavior of corrugated nano-structured surfaces”, *Nanoscale* **4**, 3937–3944 (2012).
- ²³W. Commons, *File:asperities.svg — wikimedia commons, the free media repository*, [Online; accessed 3-February-2023], 2022.
- ²⁴I. Szlufarska, M. Chandross, and R. W. Carpick, “Recent advances in single-asperity nanotribology”, *Journal of Physics D: Applied Physics* **41**, 123001 (2008).
- ²⁵G. Binnig, C. F. Quate, and C. Gerber, “Atomic force microscope”, *Phys. Rev. Lett.* **56**, 930–933 (1986).
- ²⁶S. S. Perry, “Scanning Probe Microscopy Measurements of Friction”, *MRS Bulletin* **29**, 478–483 (2004).
- ²⁷Hertz, “On the contact of elastic solids”, *Crelle’s Journal* **92**, 156–171.
- ²⁸D. Maugis, “Adhesion of spheres: the jkr-dmt transition using a dugdale model”, *Journal of Colloid and Interface Science* **150**, 243–269 (1992).
- ²⁹M. H. Müser, “Rigorous field-theoretical approach to the contact mechanics of rough elastic solids”, *Phys. Rev. Lett.* **100**, 055504 (2008).
- ³⁰B. N. J. Persson, “Theory of rubber friction and contact mechanics”, *The Journal of Chemical Physics* **115**, 3840–3861 (2001).
- ³¹J. A. Greenwood and J. B. P. Williamson, *Contact of nominally flat surfaces*, en, 1966.
- ³²A. Bush, R. Gibson, and T. Thomas, “The elastic contact of a rough surface”, *Wear* **35**, 87–111 (1975).
- ³³B. Luan and M. O. Robbins, “The breakdown of continuum models for mechanical contacts”, *Nature* **435**, 929–932 (2005).
- ³⁴Y. Dong, A. Vadakkepatt, and A. Martini, “Analytical models for atomic friction”, *Tribology Letters* **44**, 10.1007/s11249-011-9850-2 (2011).
- ³⁵E. Gnecco, R. Bennewitz, T. Gyalog, C. Loppacher, M. Bammerlin, E. Meyer, and H.-J. Güntherodt, “Velocity dependence of atomic friction”, *Phys. Rev. Lett.* **84**, 1172–1175 (2000).
- ³⁶P. Hänggi, P. Talkner, and M. Borkovec, “Reaction-rate theory: fifty years after kramers”, *Rev. Mod. Phys.* **62**, 251–341 (1990).
- ³⁷Y. Sang, M. Dubé, and M. Grant, “Thermal effects on atomic friction”, *Phys. Rev. Lett.* **87**, 174301 (2001).
- ³⁸S. Y. Krylov, K. B. Jinesh, H. Valk, M. Dienwiebel, and J. W. M. Frenken, “Thermally induced suppression of friction at the atomic scale”, *Phys. Rev. E* **71**, 065101 (2005).
- ³⁹S. Krylov and J. Frenken, “Thermal contact delocalization in atomic scale friction: a multitude of friction regimes”, *English, New Journal of Physics* **9**, 10.1088/1367-2630/9/10/398 (2007).
- ⁴⁰K. B. Jinesh, S. Y. Krylov, H. Valk, M. Dienwiebel, and J. W. M. Frenken, “Thermolubricity in atomic-scale friction”, *Phys. Rev. B* **78**, 155440 (2008).
- ⁴¹Q. Li, Y. Dong, D. Perez, A. Martini, and R. W. Carpick, “Speed dependence of atomic stick-slip friction in optimally matched experiments and molecular dynamics simulations”, *Phys. Rev. Lett.* **106**, 126101 (2011).
- ⁴²Y. Dong, Q. Li, and A. Martini, “Molecular dynamics simulation of atomic friction: a review and guide”, *Journal of Vacuum Science & Technology A* **31**, 030801 (2013).
- ⁴³K. Johnson and J. Woodhouse, “Stick-slip motion in the atomic force microscope”, *Tribology Letters* **5**, 155–160 (1998).
- ⁴⁴S. N. Medyanik, W. K. Liu, I.-H. Sung, and R. W. Carpick, “Predictions and observations of multiple slip modes in atomic-scale friction”, *Phys. Rev. Lett.* **97**, 136106 (2006).
- ⁴⁵J. Frenkel and T. Kontorova, “On the theory of plastic deformation and twinning”, *Phys. Z. Soviet.* **13** (1938).
- ⁴⁶J. Norell, A. Fasolino, and A. Wijn, “Emergent friction in two-dimensional fренkel-kontorova models”, *Physical Review E* **94**, 10.1103/PhysRevE.94.023001 (2016).

- ⁴⁷M. Dienwiebel, N. Pradeep, G. S. Verhoeven, H. W. Zandbergen, and J. W. Frenken, “Model experiments of superlubricity of graphite”, *Surface Science* **576**, 197–211 (2005).
- ⁴⁸C. Kittel, *Introduction to solid state physics*, 8th ed. (Wiley, 2004).
- ⁴⁹J. A. van den Ende, A. S. de Wijn, and A. Fasolino, “The effect of temperature and velocity on superlubricity”, *Journal of Physics: Condensed Matter* **24**, 445009 (2012).
- ⁵⁰M. Weiss and F.-J. Elmer, “Dry friction in the Frenkel-Kontorova-Tomlinson model: dynamical properties”, *Zeitschrift für Physik B Condensed Matter* **104**, 55–69 (1997).
- ⁵¹B. Bhushan, “Nanotribology and nanomechanics”, *Wear* **259**, 15th International Conference on Wear of Materials, 1–? (2005).
- ⁵²O. Penkov, H.-J. Kim, H.-J. Kim, and D.-E. Kim, “Tribology of graphene: A review”, *International Journal of Precision Engineering and Manufacturing* **15**, 577–585 (2014).
- ⁵³X. Zhao, M. Hamilton, W. G. Sawyer, and S. S. Perry, “Thermally activated friction”, *Tribology Letters* **27**, 113–117 (2007).
- ⁵⁴G Paolicelli, M Tripathi, V Corradini, A Candini, and S Valeri, “Nanoscale frictional behavior of graphene on sio₂ and ni(111) substrates”, *Nanotechnology* **26**, 055703 (2015).
- ⁵⁵S. Zhang, Y. Hou, S. Li, L. Liu, Z. Zhang, X.-Q. Feng, and Q. Li, “Tuning friction to a superlubric state via in-plane straining”, *Proceedings of the National Academy of Sciences* **116**, Publisher: Proceedings of the National Academy of Sciences, 24452–24456 (2019).
- ⁵⁶M. R. Vazirisereshk, H. Ye, Z. Ye, A. Otero-de-la Roza, M.-Q. Zhao, Z. Gao, A. T. C. Johnson, E. R. Johnson, R. W. Carpick, and A. Martini, “Origin of nanoscale friction contrast between supported graphene, mos₂, and a graphene/mos₂ heterostructure”, *Nano Letters* **19**, PMID: 31267757, 5496–5505 (2019).
- ⁵⁷H. M. Yoon, Y. Jung, S. C. Jun, S. Kondaraju, and J. S. Lee, “Molecular dynamics simulations of nanoscale and sub-nanoscale friction behavior between graphene and a silicon tip: analysis of tip apex motion.”, *Nanoscale* **7** **14**, 6295–303 (2015).
- ⁵⁸S. Li, Q. Li, R. W. Carpick, P. Gumbsch, X. Z. Liu, X. Ding, J. Sun, and J. Li, “The evolving quality of frictional contact with graphene”, *Nature* **539**, Number: 7630, 541–545 (2016).
- ⁵⁹A. Wijn, A. Fasolino, A. Filippov, and M. Urbakh, “Low friction and rotational dynamics of crystalline flakes in solid lubrication”, *Europhysics Letters (epl)* **95**, 10.1209/0295-5075/95/66002 (2011).
- ⁶⁰X. Feng, S. Kwon, J. Y. Park, and M. Salmeron, “Superlubric sliding of graphene nanoflakes on graphene”, *ACS Nano* **7**, Publisher: American Chemical Society, 1718–1724 (2013).
- ⁶¹F. Bonelli, N. Manini, E. Cadelano, and L. Colombo, “Atomistic simulations of the sliding friction of graphene flakes”, *The European Physical Journal B* **70**, 449–459 (2009).
- ⁶²M. Reguzzoni, A. Fasolino, E. Molinari, and M. C. Righi, “Friction by shear deformations in multilayer graphene”, *The Journal of Physical Chemistry C* **116**, 21104–21108 (2012).
- ⁶³Y. Liu, F. Grey, and Q. Zheng, “The high-speed sliding friction of graphene and novel routes to persistent superlubricity”, *Scientific Reports* **4**, 4875 (2014).
- ⁶⁴P. Zhu and R. Li, “Study of nanoscale friction behaviors of graphene on gold substrates using molecular dynamics”, *Nanoscale Research Letters* **13**, 34 (2018).
- ⁶⁵J. Zhang, E. Osloub, F. Siddiqui, W. Zhang, T. Ragab, and C. Basaran, “Anisotropy of graphene nanoflake–diamond interface frictional properties”, *Materials* **12**, 10.3390/ma12091425 (2019).
- ⁶⁶M. Reguzzoni and M. C. Righi, “Size dependence of static friction between solid clusters and substrates”, *Phys. Rev. B* **85**, 201412 (2012).
- ⁶⁷N. Varini, A. Vanossi, R. Guerra, D. Mandelli, R. Capozza, and E. Tosatti, “Static friction scaling of physisorbed islands: the key is in the edge”, *Nanoscale* **7**, 2093–2101 (2015).
- ⁶⁸O Zwörner, H Hölscher, U. Schwarz, and R Wiesendanger, “The velocity dependence of frictional forces in point-contact friction”, *APPLIED PHYSICS A MATERIALS SCIENCE AND PROCESSING* **66**, S263–S268 (1998).
- ⁶⁹R. Guerra, U. Tartaglino, A. Vanossi, and E. Tosatti, “Ballistic nanofriction”, *Nature Materials* **9**, 634–637 (2010).

- ⁷⁰H. Tomaç, Z. Guchan, and N. Altun, “How the stiletto heeled shoes which are popularly preferred by many women affect balance and functional skills?”, *Health Care for Women International* **43**, 1–11 (2020).
- ⁷¹K. Gibbs, *Pressure*, (2020) https://www.schoolphysics.co.uk/age16-19/Mechanics/Statics/text/Pressure_index.html.
- ⁷²F. B. Ltd, *Foot facts*, (2023) <https://www.footbionics.com/Patients/Foot+Facts.html>.